MOLECULAR PHYSICS
2020, VOL. 118, NO. 11, e1752946 (25 pages)
https://doi.org/10.1080/00268976.2020.1752946

Taylor & Francis
Taylor & Francis Group

HRMS 2019

Nuclear spin symmetry conservation studied by cavity ring-down spectroscopy of ammonia in a seeded supersonic jet from a pulsed slit nozzle

G. Wichmann, E. Miloglyadov, G. Seyfang and M. Quack

Physical Chemistry, ETH Zürich, CH-8093 Zürich, Switzerland

ABSTRACT

We report high-resolution cw laser spectra of the symmetric stretching fundamental in ammonia $^{14}NH_3$ measured with a cavity ring-down setup for mid-IR transitions (around 3300 cm^{-1}). In a supersonic jet expansion ($0.0001 \leq x(NH_3) \leq 0.04$ seeded in Ar), we have obtained rotational temperatures below 7 K. For the gas expansion, a pulsed slit nozzle with 40 mm length and 70 µm width has been used. The measured relative line intensities demonstrate that the A and E nuclear spin symmetry isomers do not interconvert in the supersonic jet expansion under these conditions (nuclear spin symmetry conservation). The lateral velocity of the gas expansion has been probed by a Doppler profile measurement, showing a preference for an expansion with an angular distribution following Lambert's cosine law perpendicular to the slit direction and an approximate molecular velocity of about 470 m/s. The experimental setup is described in detail, also in view of high-resolution spectroscopy of chiral molecules as candidates to measure the parity violating energy difference between enantiomers with a barrier to interconversion around 2500 cm^{-1}.

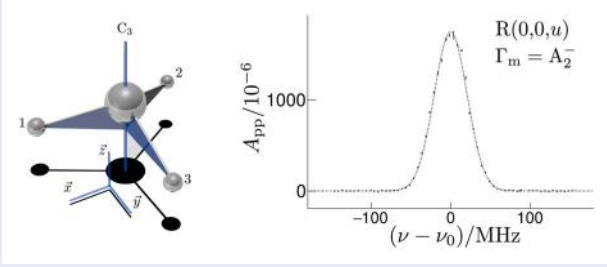

ARTICLE HISTORY
Received 6 March 2020
Accepted 19 March 2020

KEYWORDS
Nuclear spin symmetry; supersonic jet expansion; cavity ring-down absorption spectroscopy; NH_3; mid-IR high-resolution laser spectroscopy

1. Introduction

Parity and nuclear spin symmetry are approximate constants of motion which can be characterised by quantum numbers conserved in many fundamental primary processes in molecular physics, including radiative transitions, inelastic collisions and even reactions [1]. However, the underlying symmetries are not exact and are known to be broken under certain circumstances [2] and the role of fundamental symmetries and slight asymmetries is of interest in a much broader context in science and beyond [3]. Nuclear spin symmetry mixing, in particular, has been seen in a few high-resolution spectroscopic experiments on polyatomic molecules [4–6] as well as on diatomic molecules and ions [7–9] (see also the review [2]). Following the early experiments on essentially stable ortho- and para-nuclear spin isomers of hydrogen H_2 [10,11] (which can be stored for months), the common observation has been that nuclear spin symmetry isomers are relatively long-lived with only slow interconversion [12] (see, e.g. the reviews [13–15] and references therein). On the other hand, in the condensed phases, in particular in the presence of paramagnetic species, and also in low temperature matrices, nuclear spin isomer conversion is rather commonly observed [16–26]. However, when studying the populations of nuclear spin isomers after rapid cooling in supersonic jet expansions in molecular beams, nuclear spin symmetry conservation has been most commonly observed. Examples include methane ($^{12}CH_4$ [27–33] and $^{13}CH_4$ [34]), H_2O [35–38], and more recently also CH_3D, CHD_3, CH_3F and CH_3Cl [39]. Nuclear spin isomer interconversion in ammonia $^{14}NH_3$ and $^{15}NH_3$ has been recently studied theoretically

CONTACT M. Quack Martin@Quack.ch; quack@ir.phys.chem.ethz.ch Physical Chemistry, ETH Zürich, CH-8093 Zürich, Switzerland

[40]. Ammonia is of particular interest in this context as a prototypical tunnelling molecule (see [41] and references cited therein). Ammonia ($^{14}NH_3$) has also been investigated in molecular beam experiments at relatively high concentrations with some differing results [42–45] (see also [46]). Spectroscopic techniques used in these studies included high-resolution Fourier Transform Infrared (FTIR), infrared diode laser and colour centre laser spectroscopy, as well as near-infrared (NIR) diode laser cavity ring-down spectroscopy. For an extensive review of the earlier work, see [29].

In the present work, we describe an experimental setup for mid-IR very high-resolution laser spectroscopy with an optical parametric oscillator (OPO) at MHz (and potentially sub-MHz) instrumental resolution, combined with the cavity ring-down technique for achieving high sensitivity. We use the setup here to test nuclear spin symmetry conservation in NH_3 seeded at high dilution in Argon (including mole fractions $x(NH_3) < 0.0002$). The results are consistent with nuclear spin symmetry conservation under these conditions. The experimental setup can potentially also be used to study rotation-vibration-tunnelling spectra of chiral molecules at high resolution in the mid-IR, in view of experiments on molecular parity violation [2,3,47–52]. Some preliminary results of the present work were reported in [53,54]. In the following, we shall first describe the new experimental setup in some detail (see Section 2) and then explain the methodological basis for the analysis, including symmetry aspects and nomenclature (see Section 3). Results are described in Section 4, followed by a critical discussion and conclusion with an outlook.

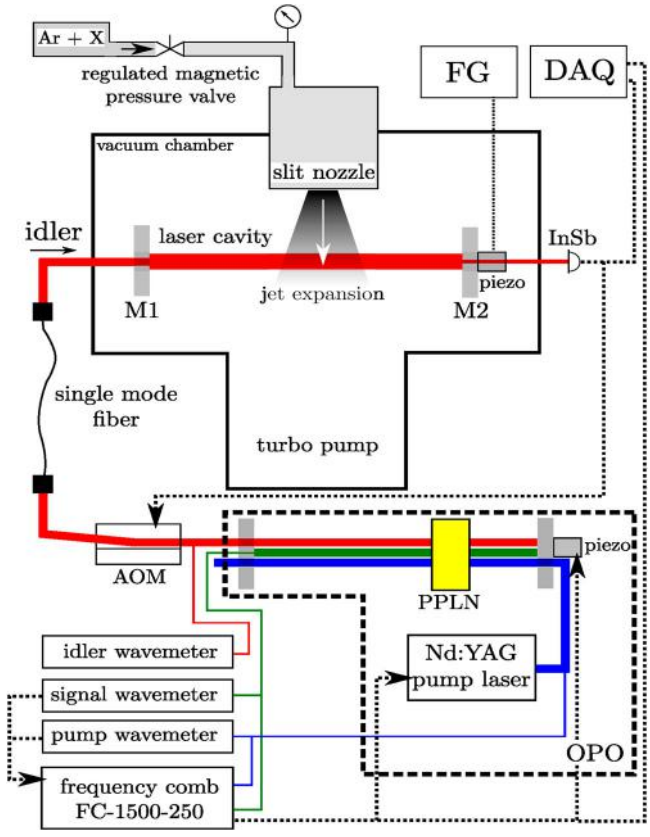

Figure 1. From left, a mid-IR cw laser 'idler' is incident onto the laser cavity. The slit nozzle is placed with expansion direction perpendicular to the cavity axis. The cavity resonance is steadily changed by a piezo shifting mirror 'M2' driven by a function generator 'FG'. When the cavity resonance is close to the incident laser frequency, the circulating power in the cavity increases. When the power reaches a threshold (detected by the transmission photo diode, 'InSb') the incident laser power is switched off using the acousto-optic modulator 'AOM' and a cavity ring-down signal is recorded as digitised by the data acquisition 'DAQ'. This is repeated for events with an open slit nozzle and with an empty cavity. The ejected gas is removed by a mechanically decoupled turbomolecular pump. The idler frequency during a ring-down is determined indirectly by the frequency comb measurement of the pump and signal frequencies.

2. Experimental

2.1. Overview of the method

The basic scheme of the experiment follows our earlier work in the near-IR [31,32,36,55,56] extended here to the mid-IR. An overview of the experiment is given in Figure 1. A single mode laser system using a cw optical parametric oscillator (OPO), with output power of about 1 W and referenced to a frequency comb, provides mid-IR photons for a laser cavity with a high finesse in the wavenumber range from 2900 cm^{-1} to 3400 cm^{-1}. The incident laser beam can be shifted by an acousto-optic modulator (AOM, 40 MHz), switching the laser on and off in less than 300 ns. The transmission through the laser cavity is recorded by an infrared detector (a liquid nitrogen-cooled InSb photodiode J10D, Judson Infrared, Inc.). When the laser radiation is switched off, the decay of the signal intensity (ring-down) is recorded [56] with

$$I(t) = I_0 \cdot e^{-t/\tau} = I_0 \cdot e^{-kt} \quad (1)$$

$$k = 1/\tau = \alpha' \cdot c + (1 - R) \cdot c/L \quad (2)$$

I_0 is the initial intensity proportional to the circulating power in the cavity, R is the reflectivity of the mirrors, L is the length of the laser cavity, c is the speed of light, τ is the lifetime of the exponential decay and α' is the absorption by the gas between the mirrors. For further background and various general aspects and applications of the cavity ring-down technique we refer to [29,31,32,55,56,57–66].

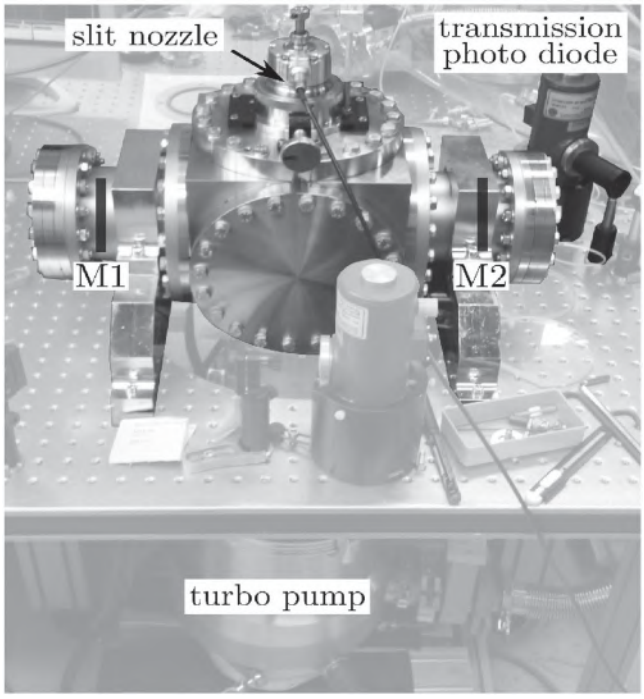

Figure 2. Photograph of the experimental setup with the vacuum chamber containing the laser cavity. The mid-IR laser (idler) is incident from the left. The cavity mirror positions inside the vacuum chamber are indicated with M1 and M2 (see also Figure 1).

A slit nozzle is placed with the expansion perpendicular to the optical axis of the laser cavity. The nozzle is opened at a repetition rate of 10 Hz for a time window of 400 µs. The trigger signal for opening the nozzle is arranged in such a way that the ring down is recorded simultaneously with the jet expansions at a fixed time with respect to the nozzle opening and only events in a time window smaller than ±20 µs are used. Recording the ring-down time τ with gas and τ_0 without gas results in the measurement of the absorbance per pass A_{pp} of NH_3 at the laser wavenumber:

$$A_{pp} = k_{gas} \cdot t_{pp} = \left(\frac{1}{\tau} - \frac{1}{\tau_0}\right) \cdot L/c = \alpha' \cdot L = \alpha_0 \frac{L_{Slit}}{L} \cdot L \tag{3}$$

$t_{pp} = L/c$ is the time per pass, k_{gas} is the change of the exponential decay constant caused by the sample absorption (i.e. NH_3), α_0 is the absorption coefficient of the sample, and L_{Slit} is the length of the slit nozzle. Figure 2 shows a photograph of the setup.

In Section 2.2, we describe in detail the properties of the laser cavity and the OPO cw laser and their synchronisation, and in Section 2.3, we describe the slit nozzle.

2.2. Ring-down cavity

The expansion chamber consists of a steel cube with 200 mm length and two additional tubes with mirror holders attached on flanges at the ends, resulting in a mirror distance of around 330 mm, corresponding to a free spectral range of ∼ 450 MHz. Two identical mirrors with a 1 m radius of curvature from Los Gatos Research, Inc. (LGR) are used. The waist of the fundamental cavity mode is about 0.6 mm. One mirror is placed on a ring piezo stack. This mirror is moved back and forth such that the resonance frequency of the cavity is smoothly changed for a fixed laser frequency.

If the cavity is resonant with the laser frequency, the power circulating in the cavity increases until a threshold is reached. This triggers the AOM, which switches the incident laser off. The switching off is completed (< 10% intensity) in less than 300 ns. The ring-down time of the empty cavity varies from 0.5 µs to 4 µs depending on the exact laser wavenumber between 2900 cm^{-1} and 3400 cm^{-1}, determined by the wavenumber-dependent mirror reflectivity. The maximum enhancement factor of the cavity is about 2500 and an in-coupling of 10% with an incident laser power of 20 mW was achieved. Therefore, for a beam waist of $w \approx 0.6$ mm, the maximum of the peak intensity in the cavity is about 1 kW/cm^2. The infrared laser is an optical parametric oscillator (Qioptic, Kilo). A single mode cw Nd-YAG laser (MOPA Inno light GmbH, ≃ 20 W, 1064 nm) is used as pump laser, and split into signal and idler beams by a periodically poled lithium niobate (PPLN) crystal with the signal beam enhanced by a cavity. Changing the periodicity of the PPLN makes it possible to vary the wavelength of the signal from 1.4 µm to 2 µm and of the idler from 2.3 µm to 4.6 µm. Both signal and idler have an output power larger than 0.5 W. The pump laser and the signal are referenced to a frequency comb with an Allen deviation $\sigma_{\Delta\nu}(1s)$ smaller than 30 Hz for the experiment. The uncertainty of the stabilised idler frequency is estimated, by the width of the beat signal with the frequency comb, to be smaller than 250 kHz, which is small compared to the Doppler width of the spectral lines observed in the supersonic jet, which is here typically about $\Delta\nu_D = 60$ MHz (FWHM, full width at half maximum).

During a measurement the laser is set to a fixed frequency. After a start trigger (start time t_0) the cavity mirror is moved with a constant speed in one direction and returns with a constant speed, resulting in a triangular shape for the displacement (labelled 'applied piezo voltage' in Figure 3). When the cavity is resonant, the signal on the photo diode increases and is detected as an intensity peak (labelled 'transmission signal'). With an additional logical gate (labelled 'mode selection window')

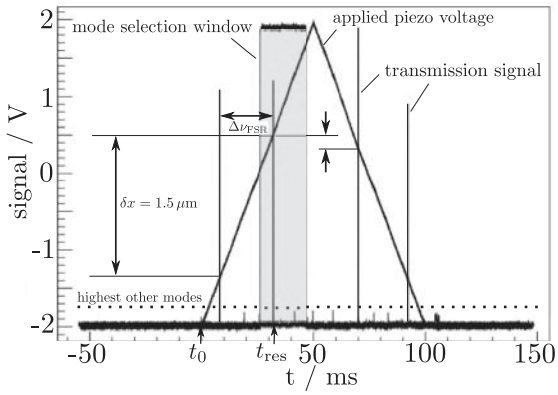

Figure 3. Applied piezo voltage function (not to scale) and the corresponding cavity transmission signal. The cavity is driving more than one free spectral range ($\Delta\nu_{FSR}$), which corresponds to a mirror displacement of 1.5 µm ($= \lambda_{idler}/2$) with an actual mirror speed of 1.5 µm/22 ms $=$ 0.07 mm/s.

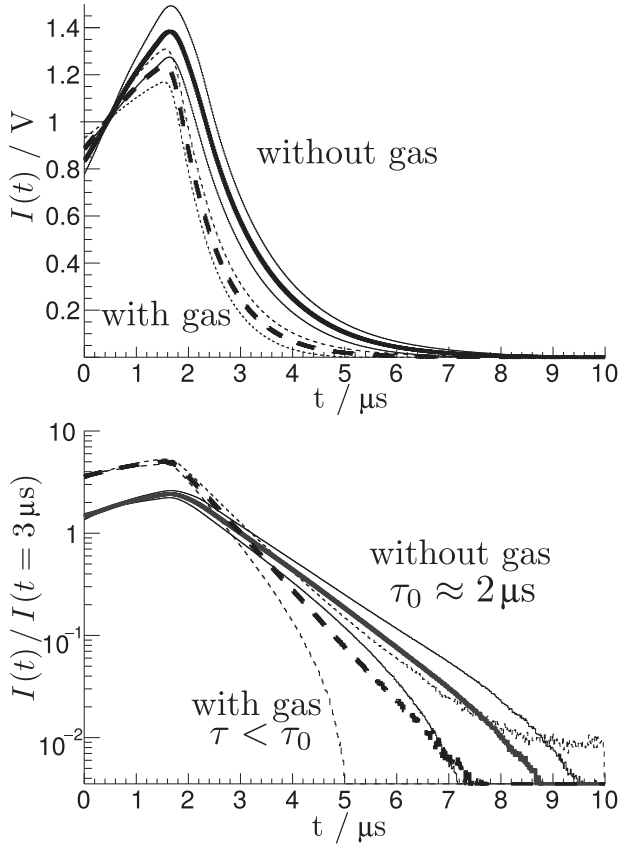

Figure 4. *Top*: This shows the average of 1000 cavity ring-down signal functions $I(t)$ with and without gas jet between the laser mirrors. $I(t)$ is the electrically amplified signal from the InSb transmission diode. The average trace is bounded by traces of one standard deviation of 1000 signal functions. *Bottom*: The same information is presented normalised to the intensity at 3 µs after the trigger signal for the AOM. The slopes of the two lines in this logarithmic representation correspond to the decay times with $\ln[I(t)/I(t = 3\mu s)] \propto -t/\tau = -kt$.

the same cavity mode is always selected, also with the same direction of the mirror movement. This is necessary to obtain the time t_{res} when the selected mode is resonant after the start time t_0. Then, t_{res} is used for the next start trigger to estimate the optimum time to open the slit nozzle, which must be around $t_{res} - 2$ ms. Since the last t_{res} is used for the next estimate, any slow changes of the cavity by temperature or drifts of the piezo are compensated for. This scheme can independently change the piezo speed and the repetition rate for the slit nozzle opening. In this way, the cavity ring-down is recorded (see Figure 4) and by repetition for different laser frequencies the line shape is obtained (see Figures 16 and 14 in the results, Section 4).

2.3. Slit nozzle

Figure 5 shows a sketch of the slit nozzle. The nozzle is made of stainless steel with a thickness of 0.5 mm. A slit of 40 mm length has been created using wire erosion, resulting in a constant width measured to be about 70 µm with an uncertainty of ±15 µm (see Figure 6). The usual arrangement is such that the laser cavity mode is aligned along the slit nozzle at a distance $H \approx 5$ mm below the slit. The angle $\Theta = 0°$ defines the vertical direction and $\Theta = \pm 90°$ the horizontal direction. The angle γ is the misalignment between the slit nozzle ($\vec{X}$ direction) and the optical axis of the cavity. The pressure p_0 of the gas before expansion is regulated to 1.5 ± 0.02 bar. The average background pressure p_1 of the chamber during 20 Hz operation is below 10^{-3} mbar. Special care has been taken in the design of the sealing plunger.

To reduce the necessary lifting force, the plunger is designed with low mass using polyether ether ketone (PEEK). The lateral stabilisation of the plunger is achieved with two ball bearings to ensure low friction. Instead of a solid rubber sealing, a hollow silicone tube has been used. The tube gives the advantage of lower mass, less adhesion to the steel and most importantly an increased deformability resulting in a lower force needed to seal the slit.

To drive the slit nozzle, an electro-magnetic driver from Parker Instruments is used. To open the slit nozzle, a square function with an amplitude of approximately 300 V and a duration of 0.5 ms is applied to a coil with about 60 mH, lifting the sealing upwards. Figure 7 shows the effective absorption per pass (A_{pp}) for a fixed frequency but for different delay times between the opening of the slit nozzle and recording of the cavity ring-down signal. The opening time is about 400 µs, while the recorded ring-down time is less than 10 µs (see also Figure 4). To determine the ring-down time less than

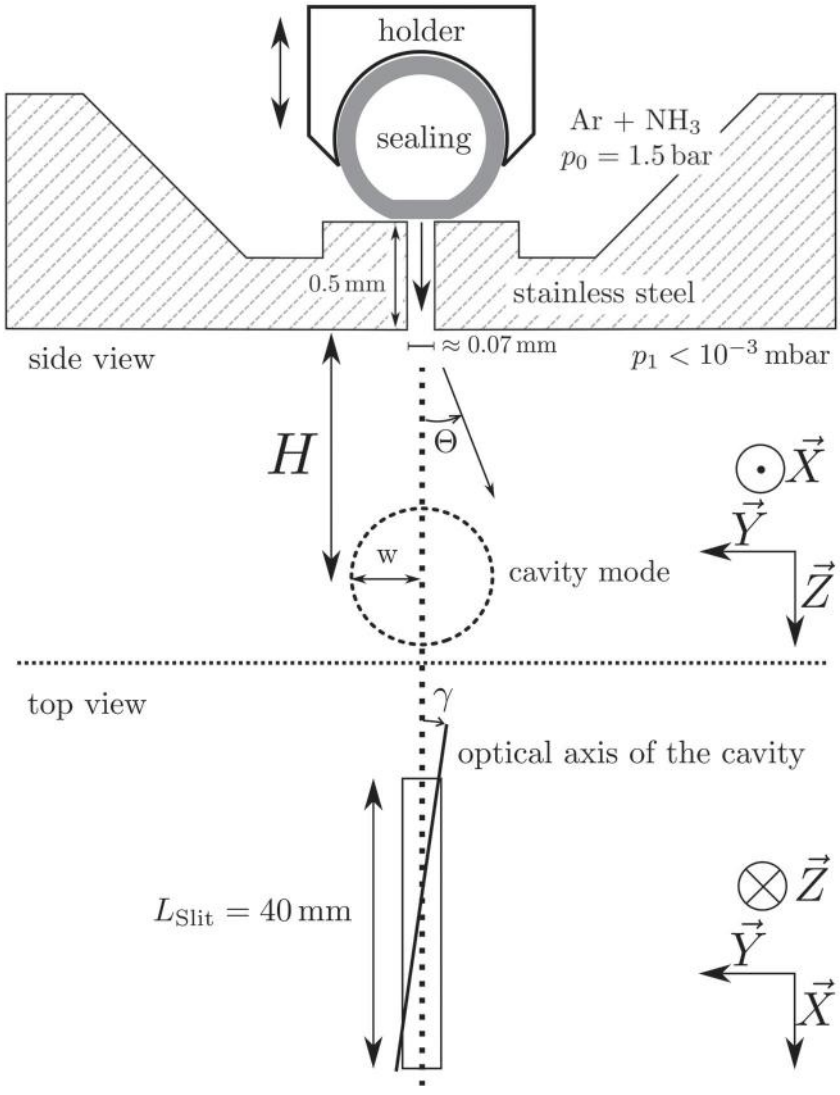

Figure 5. The slit nozzle is 40 mm long and has an opening of 70 µm with an uncertainty of ±15 µm. A plunger is placed on top, which is pressed by springs against the opening and can be lifted by an electrical pulse. It consists of a holder made out of PEEK for reduced weight and a hollow silicone tube for sealing instead of a solid rubber reducing the pressure necessary for deformation, i.e. for sealing. The cavity mode, with waist size around $w \approx 0.6$ mm, is aligned parallel to the slit nozzle at a distance $H \approx 5$ mm below the slit. The angle $\Theta = 0^\circ$ is defined as the vertical direction and $\Theta = \pm 90^\circ$ as the horizontal direction. The angle γ is the misalignment between the length axis of the slit nozzle and the centre axis of the laser cavity mode.

2 µs from the transmission signal is used. Within these short times, the density of the gas from the pulse varies by less than 1%. Furthermore different measurements compare results from practically the same density profile and therefore the effect nearly cancels in relative line intensity measurements.

In order to characterise the jet expansion, we have measured the Doppler profile with the slit nozzle rotated by $\gamma = 90^\circ$. The expansion velocity of the molecules has been estimated by comparing with a simulation. The simulation uses a Gaussian velocity distribution with mean $\bar{v}_{NH_3}$ and a standard deviation of $\sigma_v = 0.15 \cdot \bar{v}_{NH_3}$ independent of the gas emission angle Θ. For $\gamma = 90^\circ$ and $\beta = v/c < 10^{-5}$, when neglecting the movement in the $\vec{x}$ direction, the calculated Doppler shift of a single molecule is $\Delta\nu_D \approx \nu_0 \cdot \beta \cdot \sin\Theta$. For each assumed trajectory, a random start position in the plane of the slit nozzle exit, a velocity v and an angle Θ for the flight direction was chosen. With these three random variables, the intra-cavity laser intensity for this trajectory is defined and the individual absorption probability is calculated using the Runge Kutta method. By sampling over 10^5 different trajectories, the simulated Doppler profile is obtained.

The molecular transit time through the laser beam depends on Θ and results in an additional Θ-dependence

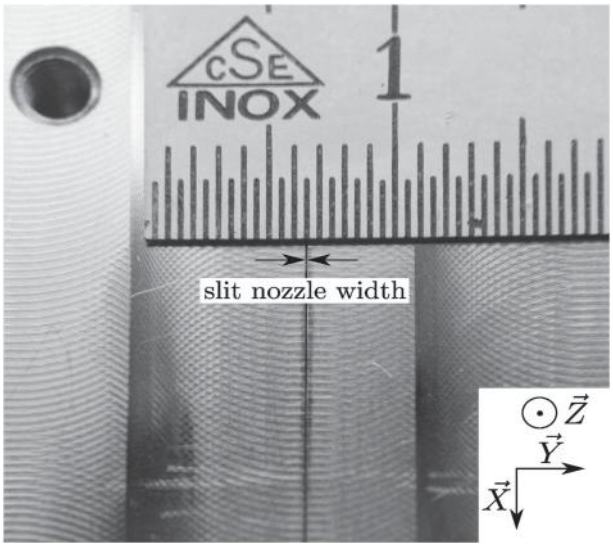

Figure 6. The vertical line below 6.5 mm is the slit nozzle. From this image (with higher resolution), the width can be estimated to be 70 µm with an uncertainty of ±15 µm.

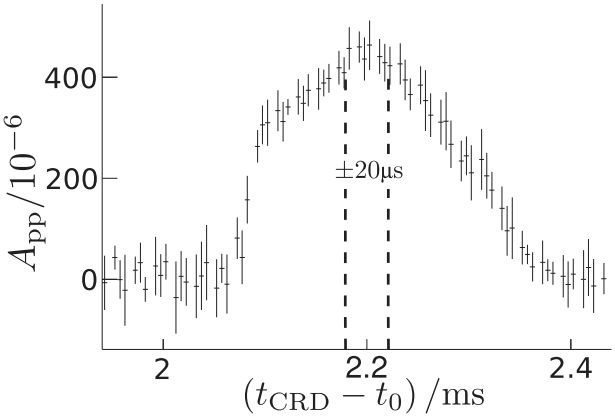

Figure 7. Measured absorbance per pass versus the time between the start trigger t_{CRD} of the cavity ring-down (AOM trigger time) minus the slit nozzle trigger t_0. This diagram shows the time scale of the mechanical opening and closing process of the slit nozzle. Only the time window with maximum absorption ±20 µs is used for the line shape measurements.

of the calculated absorption profile. Three simulated line shapes are given in Figure 8 using the differential emission probabilities $dn \propto d\Theta$, $dn \propto \cos\Theta d\Theta$ and $dn \propto \cos^2\Theta d\Theta$, with $\int_{\Theta}^{\Theta+d\Theta} dn(\Theta)$ being the number density of ejected particles into the direction $[\Theta, \Theta + d\Theta]$. The approximate agreement of the experiment with the simulation in Figure 8 demonstrates that the Ar-NH_3 mixture is ejected presumably following Lambert's cosine law with $dn \propto \cos\Theta\, d\Theta$. The simulation results in a Gaussian distribution with mean $\bar{v}_{NH_3} = 472.5(5)$ m/s and a full width at half maximum $\sigma_v \cdot 2\sqrt{2\ln 2} = 167$ m/s for the absolute gas velocity ejected from the slit nozzle. A

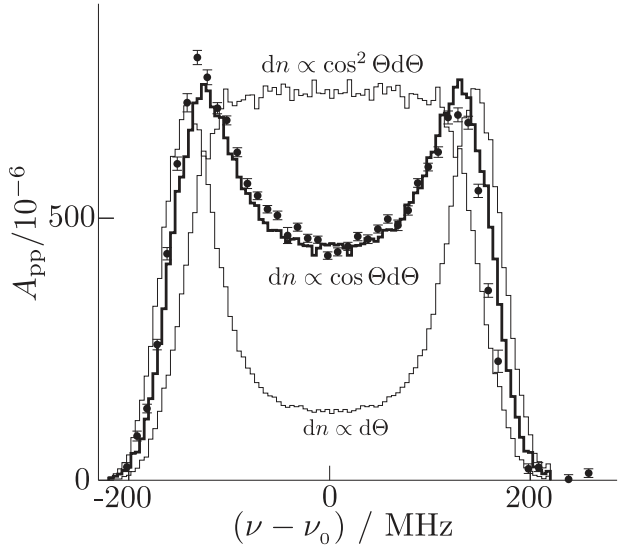

Figure 8. Measured Doppler shift of the slit nozzle with the laser mode perpendicular to the direction of the slit ($\gamma = 90°$). Three different gas emission distributions are shown for illustration (dn ∝ dΘ, dn ∝ cos ΘdΘ and dn ∝ cos² ΘdΘ). Assuming the best fit with Lambert's cosine law (dn ∝ cos ΘdΘ) and assuming a Gaussian velocity spread of $\sigma = 15\%$, an exit velocity of 472.5(5) m/s is obtained (bold line), and the simulation agrees well with the measurements shown as points with error bars.

simple model assumption, which assumes that all the internal energy of the mixture before the expansion is transferred to translation in z-direction, gives the upper bound $v_z^{relaxed} = \sqrt{2kT_0\gamma'/((\gamma'-1)m)} = 556$ m/s [29, Equation (3)] (with $T_0 = 300$ K, $\gamma' = C_p/C_V = 5/3$, and $m = m_{Ar}$).

In Figure 9, the integrated line strength $\bar{A}$ (and simultaneously the full width at half maximum, FWHM of the spectral line) was measured for different distances H between the centre axis of the laser cavity mode and the slit nozzle opening for the transition Q(2,2,l) of NH_3 (see Section 4 for the notation 'Q(2,2,l)' and for '$\bar{A}$' see Equation (18) in Section 3). This dependence does not represent the gas density directly, since the rotational temperature and therefore the population of the initial state is not independent of H. With increasing H the rotational temperature decreases (and hence also the population of the probed initial excited rotational state), and hence the density for larger H is higher than indicated by the measured effective line strength.

2.4. Sample preparation

We always used mixtures of Ar and NH_3. The ammonia gas is from Aldrich Chemistry with a stated purity > 99.98% of NH_3 with natural isotopic abundances. The Argon is a 200 bar gas bottle from PanGas with a stated purity > 99.998%. The samples for the supersonic jet

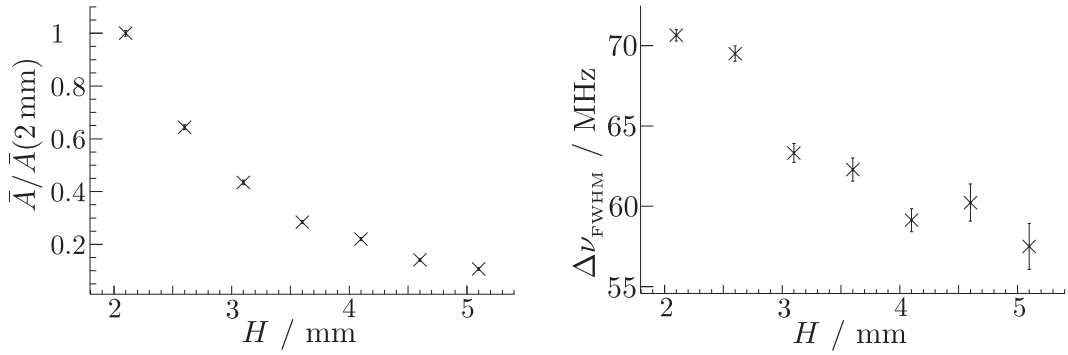

Figure 9. *Left*: The distance H between the centre axis of the laser cavity mode and the slit nozzle opening was varied and the decrease of the molecular density of the NH_3 molecules in the state ($J = 2$, $K = 2$, $v = (0)^l$, $\Gamma_m = E^+$) was obtained by integration over the measured line absorbance for the transition Q(2,2,*l*) (see Sections 3 and 4 for the notation). *Right*: The FWHM decreases with H.

expansion were prepared with serial dilution as follows: a 0.5 l gas bottle was filled with NH_3 to a pressure p_1 and then the pressure was increased to p_2 with Ar. Subsequently, a part of the mixture was removed, resulting in a new pressure p_1', which was then again increased with Ar to p_2'. This procedure was repeated until the desired concentration range was reached. In the last step, an empty 20 l gas bottle was connected, reducing the pressure by about a factor 40, and again filled with Ar. The last step resulted in a larger amount of sample for repeated measurements at the same mixture concentration. For $x(n_{NH_3}) < 10^{-3}$ four dilution steps were used. In each step, p_1 and p_2 were measured with a pressure gauge (PNI024, ifm electronic) with a systematic uncertainty of $\pm 0.6\%$ resulting in the uncertainty estimate given. The actual concentration of NH_3 in the final mixture available for expansion may be somewhat different from the calculated values because of adsorption effects. Therefore, for each mixture a unique mixture ID is introduced in Table 1 and quantitative comparisons of different line intensities are restricted to the same mixture only (see Section 4). The average consumption of sample gives an upper limit of 0.019 ml for the amount of gas per pulse (with a pressure $p_0 = 1.5$ bar before expansion).

Table 1. Table of the sample mixtures $x(NH_3) = n(NH_3)/(n(Ar) + n(NH_3)) \simeq n(NH_3)/n(Ar)$ for small x.

ID	$x(NH_3)$	ID	$x(NH_3)$
1:	0.0007(2)	7:	0.006(1)
2:	0.015(1)	8:	0.0090(8)
3:	0.00010(2)	9:	0.022(3)
4:	0.0012(3)	10:	0.036(3)
5:	(small)	11:	0.008(1)
6:	0.010(2)	12:	0.000100(2)

Notes: The stated mixture uncertainty in parentheses is determined by the pressure gauge uncertainty and error propagation for the dilution process. Additional uncertainties are caused by the unknown adsorption to the container walls during the mixture process. Therefore, the fractions given are only semiquantitative statements for the mixtures. For each mixture, a unique mixture ID is introduced and quantitative comparisons of different line intensities are restricted to the same mixture. ID 5 corresponds to a small but uncertain value due to desorption effects.

3. Level structure, nuclear spin symmetry and parity in NH_3

NH_3 is a symmetric top molecule of C_{3v} point group symmetry in its equilibrium geometry in the electronic ground state, as shown in Figure 10, with the z-axis along the C_3 symmetry axis. As is well known, NH_3 has a low barrier to inversion through the D_{3h} transition structure, resulting in easily resolved large tunnelling splittings of about 0.7 cm^{-1}, depending upon the rotational and vibrational state. Therefore, the rotation-vibration-tunnelling sublevels can be classified in the molecular symmetry group following Longuet–Higgins [67], which in the present case is identical to the full permutation–inversion group $S_3^* = S_3 \otimes S^*$. This is the direct product of the symmetric group S_3 of the permutations of the three protons and the inversion group S^* following the notation of [1,2]. $S_3{}^*$ is isomorphous to the point group D_{3h} of the planar transition structure, which in this particular case can be used equivalently to classify the rotation-vibration-tunnelling levels. This has in fact been widely used in this context [68]. We note, however, that this procedure is not generally applicable. It would not work for methane CH_4, for example (see [2] for a detailed discussion). Table 2 provides the character table and various notations used for the irreducible representations of the isomorphous groups. We use the systematic notation of [1] (see also [2]), which assigns a unique symbol for the irreducible representations of S_3 (either as a partition or a letter symbol) and gives parity by a superscript '+' for positive parity or '−' for negative parity. The 2^3 nuclear spin functions for the three protons (fermions) generate a reducible representation D_R

$$D_R = 4A_1^+ + 2E^+ \tag{4}$$

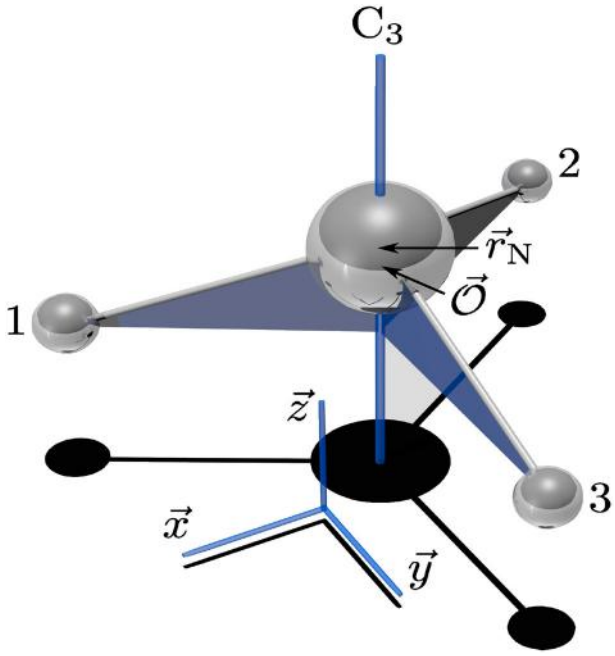

Figure 10. Perspective illustration of NH_3 in its equilibrium geometry showing the axis convention with the threefold symmetry axis (C_3) of the molecule along the *z*-direction. The three protons are labelled with '1', '2' and '3' (cf. Table 2). The origin $\vec{\mathcal{O}}$ of the molecule-fixed coordinate system ($\vec{x}$, $\vec{y}$, $\vec{z}$) is set to the centre of mass (shifted in the figure for better visualisation) and hence the position vector of the nitrogen atom $\vec{r}_N$ is on the $\vec{z}$-axis. The $\vec{y}$, $\vec{z}$-plane is chosen such that proton '3' lies in it (graphics from Blender GPL Software).

where the four A_1^+ functions correspond to the total nuclear spin $I(H_3) = 3/2$ (with $-3/2 \le M_I \le +3/2$) and the two E^+ functions correspond to $I(H_3) = 1/2$ (with $M_I = \pm 1/2$). We shall write also the total spin multiplets as ${}^4A_1^+ + {}^2E^+$.

The motional species Γ_m combine with the nuclear spin species Γ_{ns} to form the only Pauli-allowed species $A_2^\pm$, i.e. $\Gamma_m \otimes \Gamma_{ns} = A_2^\pm$ ($+\cdots$ Pauli forbidden terms, if any). Therefore, the motional species A_2^+ and A_2^- occur with nuclear spin species A_1^+ and $I(H_3) = 3/2$ and the motional wavefunctions E^+ and E^- occur with nuclear spin species E^+ ($I(H_3) = 1/2$). The $A_1^\pm$ motional species have no Pauli-allowed partner and thus do not occur for NH_3. They do occur for ND_3 (see [69]). The motional rotation-vibration species in C_{3v} can be obtained in a standard way (see [70,71]) as for rigid molecules, and the tunnelling sublevels for each level are obtained from the induced representation $\Gamma(C_{3v}) \uparrow S_3^*$ using the Frobenius reciprocity theorem and the subduced representation $\Gamma(S_3^*) \downarrow M_{S6}(C_{3v})$ given in Table 2 as well (see also [1,2] for details). With this, one obtains the rotational level symmetries for a totally symmetric vibrational state (ground state $(0)^{l,u}$ and excited state $(1)^{l,u}$ relevant here) given in Table 3 [46], which also indicates the common notation, (s, a) for pure inversion (vibration-tunnelling) symmetry or parity as symmetric (s) and antisymmetric (a) [69]. In the present work, an additional statistical weight of 3 arises because we do not resolve the hyperfine structure, neither for H nor for the quadrupole nucleus

Table 3. Notation for symmetry species in the totally symmetric vibrational (in particular ground state) level for rotational quantum numbers J and K and nuclear spin statistical weights g_{ns} (including the nuclear spin $I = 1$ for ^{14}N, see also [69] for ND_3, where all levels are Pauli-allowed and have non-zero nuclear spin statistical weights).

Γ_{vt}	Γ_m	J	K	g_{ns}	$I(H_3)$	Γ_{ns}	$\Gamma_{tot} = \Gamma_m \otimes \Gamma_{ns}$
s,a	A_1^+,A_1^-	all	3,6,9,12,... [(a)]	0	–	–	–
s,a	A_2^+,A_2^-	all	3,6,9,12,...	12	3/2	A_1^+	A_2^+,A_2^-
s,a	E^+,E^-	all	1,2,4,5,... [(b)]	6	1/2	E^+	A_2^+,A_2^-
a	A_1^-	odd	0	0	–	–	–
a	A_2^-	even	0	12	3/2	A_1^+	A_2^-
s	A_1^+	even	0	0	–	–	–
s	A_2^+	odd	0	12	3/2	A_1^+	A_2^+

Notes: In the first column, the pure vibrational-tunnelling symmetry or parity is indicated with the frequently used notation s and a (symmetric or antisymmetric). In the second column, the motional species of the level with $A_{1,2}^\pm$, $E^\pm$ and in the column with $I(H_3)$ the total nuclear spin for the 3 protons are given. Thus all states with $K = 3n$ have $I(H_3) = 3/2$ and all states with $K \neq 3n$ have $I(H_3) = 1/2$ (with n a positive integer and the special case $K = 0$ as indicated, see also footnotes (a) and (b)).

(a) The K-doublets ($A_1 + A_2$) have positive rotational parity for $K = 6, 12, 18\ldots$ ($K = 3n$, n even) and negative rotational parity for $K = 3, 9, 15\ldots$ ($K = 3n$, n odd).

(b) The rotational parity is positive for $K = 2, 4, 6, \ldots$ (even) and negative for $K = 1, 5, 7\ldots$ (odd).

Table 2. Character table of the symmetry group S_3^* for the NH_3 (ND_3) isotopomers (compared to D_{3h}).

		D_{3h} (class):	E	$2C_3$	$3C_2$	σ_h	$2S_3$	$3\sigma_v$		
	Species	S_3^* (class):	E	2(123)	3(12)	E*	2(123)*	3(12)*		
$\Gamma[S_3^*]$		$\Gamma[D_{3h}]$							$\Gamma(S_3^*) \downarrow S_2{}^*$	$\Gamma(S_3^*) \downarrow M_{S6}(C_{3v})$
$[3]^+$	A_1^+	A_1'	1	1	1	1	1	1	A^+	A_1
$[1^3]^+$	A_2^+	A_2'	1	1	−1	1	1	−1	B^+	A_2
$[2,1]^+$	E^+	E'	2	−1	0	2	−1	0	$A^+ + B^+$	E
$[3]^-$	A_1^-	A_1''	1	1	1	−1	−1	−1	A^-	A_2
$[1^3]^-$	A_2^-	A_2''	1	1	−1	−1	−1	1	B^-	A_1
$[2,1]^-$	E^-	E''	2	−1	0	−2	1	0	$A^- + B^-$	E

Notes: The first three columns provide species following three different notations. 1: $[\text{partition}]^{\text{parity}}$, 2: $[S_3 \text{ species}]^{\text{parity}}$, 3: D_{3h} point group species (see text and [1,2,46]).

Table 4. Vibrational energy levels of NH_3 below 3500 cm^{-1} with 'ν_1' the symmetric stretching, 'ν_2' the symmetric bending, 'ν_3' the degenerate stretching and 'ν_4' the degenerate bending vibration.

State v		Γ_{vt}	g_v	Experiment [75,76] E/(hc · cm^{-1})	Theory [72] E/(hc · cm^{-1})	p(v)	$Q^{rot,ns}$(v)
gs^l	$(0,0,0,0)^l$	A_1^+	1	−0.79	−0.75	0.496	830.998
gs^u	$(0,0,0,0)^u$	A_2^-	1	0.00	0.00	0.494	818.794
ν_2^l	$(0,1,0,0)^l$	A_1^+	1	931.64	931.52	$5.33{\cdot}10^{-3}$	9.286
ν_2^u	$(0,1,0,0)^u$	A_2^-	1	967.33	965.47	$4.48{\cdot}10^{-3}$	7.842
$2\nu_2^l$	$(0,2,0,0)^l$	A_1^+	1	1596.96	1600.70	$2.10{\cdot}10^{-4}$	–
ν_4^l	$(0,0,0,1)^l$	E^+	2	1625.48	1627.70	$3.66{\cdot}10^{-4}$	–
ν_4^u	$(0,0,0,1)^u$	E^-	2	1626.62	1628.58	$3.64{\cdot}10^{-4}$	–
$2\nu_2^u$	$(0,2,0,0)^u$	A_2^-	1	1881.38	1878.24	$5.27{\cdot}10^{-5}$	–
$3\nu_2^l$	$(0,3,0,0)^l$	A_1^+	1	2383.38	2380.28	$4.59{\cdot}10^{-6}$	–
$(\nu_2+\nu_4)^l$	$(0,1,0,1)^l$	E^+	2	2539.26	2559.71	$4.31{\cdot}10^{-6}$	–
$(\nu_2+\nu_4)^u$	$(0,1,0,1)^u$	E^-	2	2585.33	2598.73	$3.44{\cdot}10^{-6}$	–
$3\nu_2^u$	$(0,3,0,0)^u$	A_2^-	1	2894.82	2888.06	$3.82{\cdot}10^{-7}$	–
$2\nu_4^l$	$(0,0,0,2)^l$	A_1^+	1	3215.31	3220.12	$8.05{\cdot}10^{-8}$	–
$2\nu_4^u$	$(0,0,0,2)^u$	A_2^-	1	3216.99	3221.34	$7.99{\cdot}10^{-8}$	–
$(2\nu_2+\nu_4)^l$	$(0,2,0,1)^l$	E^+	2	–	3221.78	$1.56{\cdot}10^{-7}$	–
$2\nu_4^l$	$(0,0,0,2)^l$	E^+	2	3239.65	3247.97	$1.43{\cdot}10^{-7}$	–
$2\nu_4^u$	$(0,0,0,2)^u$	E^-	2	3240.83	3246.12	$1.42{\cdot}10^{-7}$	–
ν_1^l	$(1,0,0,0)^l$	A_1^+	1	3335.31	3334.00	$4.49{\cdot}10^{-8}$	–
ν_1^u	$(1,0,0,0)^u$	A_2^-	1	3336.30	3334.86	$4.47{\cdot}10^{-8}$	–
ν_3^l	$(0,0,1,0)^l$	E^+	2	3442.83	3445.10	$5.33{\cdot}10^{-8}$	–
ν_3^u	$(0,0,1,0)^u$	E^-	2	3443.19	3445.24	$5.32{\cdot}10^{-8}$	–
$4\nu_2^l$	$(0,4,0,0)^l$	A_1^+	1	3447.21	3452.33	$2.61{\cdot}10^{-8}$	–

Notes: 'p(v)' is the population of the vibrational-tunnelling state at 296 K including the twofold degeneracy of all E-symmetric states and using the stated experimental energies from [75]. The values for $3\nu_2$ and $4\nu_2$ are taken from [76] and the theoretical value is used for the missing combination band $2\nu_2+\nu_4$. The vibrational-tunnelling partition function is calculated to $Q_{vib.tun.} = 2.026$. The rotational partition function including the nuclear spin for the vibrational ground state is $Q^{rot,ns}((0)^l) = 830.998$, including all rotational states up to $J \le 20$, i.e. $\approx 4000\,cm^{-1}$ (see Equation (13)). For the here most frequently used vibrational-tunnelling states the short-hand notations $(0)^{l,u} = (0,0,0,0)^{l,u}$ and $(1)^{l,u} = (1,0,0,0)^{l,u}$ are used elsewhere in this publication.

^{14}N ($I^\pi = 1^+$). As the ^{14}N nucleus has positive parity the Γ_{tot} also give the total parity including ^{14}N. For the nucleus $^{15}N(I^\pi = (1/2)^-)$ the parity of each level will be reversed.

A survey of the vibrational-tunnelling and rotational level structures without hyperfine structure is given in Tables 4 and 5. The states are distinguished by the rotational quantum numbers J, K, and the vibrational-tunnelling state $\mathbf{v} \equiv (v_1, v_2, v_3, v_4)^i$ with $i = (u \text{ or } l)$ for the upper or the lower state of the corresponding vibrational-tunnelling states (similar to Ref. [72]). From this simplification, one has for a state $(J, K, \mathbf{v})$ the total degeneracy factor

$$g(J,K,\mathbf{v}) = (2J+1)\cdot g_{ns}(J,K,\mathbf{v})\cdot g_v \qquad (5)$$

Here the nuclear spin degeneracy (and $\Gamma_m(J,K,\mathbf{v}) = \Gamma_{rot}\otimes\Gamma_{vib}\otimes\Gamma_{tun}$) is

$$g_{ns}(J,K,\mathbf{v}) = \begin{cases} 6, & \text{if } \Gamma_m = E^\pm \\ 12, & \text{if } \Gamma_m = A_2{}^\pm \end{cases} \qquad (6)$$

The vibrational degeneracy is g_v, noting that rotation and vibration are not rigorously separable [41].

The notation for an energy level of the state $(J, K, \mathbf{v})$ is then $E_{J,K,\mathbf{v}}$ (to be distinguished from the non-italic letters for the irreducible representations $E = \{E^+, E^-\}$ or $A = \{A_1^\pm, A_2^\pm\}$). Almost all of these levels are known from accurate measurements [73–76, and references cited therein]. We compare also with the results from theory [41,72]. Strictly speaking, experiments on NH_3 have obtained only accurate relative energies within each nuclear spin isomer because so far no transitions between levels of different nuclear spin symmetry (A and E) have been obtained. This situation is very common in spectroscopy because the energy levels for different nuclear spin symmetries behave as separate isomers. Only in a few cases has the 'isomerisation energy' been measured directly. However, at a lower level of spectroscopic accuracy than is available within the states of the same nuclear spin symmetry, one can derive the 'nuclear spin isomerisation energy' from a joint effective Hamiltonian fit to the spectra of the two (or more) nuclear spin isomers or also if the dissociation energy to a common dissociation channel has been measured. The approximate experimental energy difference from a joint effective Hamiltonian fit for NH_3 ($\Delta E = E^l_{1,1,(0)} - E^u_{0,0,(0)} = 15.379(hc)\,cm^{-1}$) agrees quite well with the corresponding difference obtained from theory with $15.391\,cm^{-1}$ (see Table 5). We draw attention here also to the exceptionally accurate recent determination of the ortho-para interval in H_2 [77].

To calculate the expected line intensities, we first consider the state population with and without nuclear spin conservation after the jet expansion (**n**uclear spin

Table 5. For different effective rotational temperatures T_{rot}, all populations p with energy E smaller than 200(hc) cm^{-1} above the ground state $J = K = 0, A_2^-, (0,0,0,0)^u$ (abbreviated as $(0)^{u,l}$ for the upper and lower tunnelling levels) are calculated with nuclear spin symmetry relaxation 'nr' from Equation (10), and with nuclear spin symmetry conservation 'nc' from Equation (11).

							T_{rot} = 6.6 K		T_{rot} = 10 K		T_{rot} = 77 K		T_{rot} = 296 K
J	K	Γ_m	g	E^a/(hc · cm^{-1})	E^b/(hc · cm^{-1})	v	p_{nr}	p_{nc}	p_{nr}	p_{nc}	p_{nr}	p_{nc}	p_{nr}
0	0	A_1^+	0	–	−0.751	$(0)^l$	–	–	–	–	–	–	–
0	**0**	**A_2^-**	**12**	**0.000**	**0.000**	$(0)^u$	0.874	0.475	0.661	0.417	0.052	0.051	0.007
1	**1**	**E^-**	**18**	**15.379**	**15.391**	$(0)^l$	0.046	0.272	0.108	0.257	0.058	0.058	0.010
1	**1**	**E^+**	**18**	**16.169**	**16.139**	$(0)^u$	0.039	0.229	0.097	0.230	0.057	0.057	0.010
1	**0**	**A_2^+**	**36**	**19.096**	**19.095**	$(0)^l$	0.041	0.022	0.127	0.080	0.108	0.108	0.020
1	0	A_1^-	0	–	19.837	$(0)^u$	–	–	–	–	–	–	–
2	**2**	**E^+**	**30**	**44.002**	**43.965**	$(0)^l$	$1.5{\cdot}10^{-4}$	$8.8{\cdot}10^{-4}$	0.003	0.007	0.057	0.057	0.015
2	2	E^-	30	44.793	44.715	$(0)^u$	$1.3{\cdot}10^{-4}$	$7.4{\cdot}10^{-4}$	0.003	0.006	0.056	0.056	0.014
2	**1**	**E^-**	**30**	**55.144**	**55.069**	$(0)^l$	$1.3{\cdot}10^{-5}$	$7.8{\cdot}10^{-5}$	$5.9{\cdot}10^{-4}$	$14.0{\cdot}10^{-4}$	0.046	0.046	0.014
2	1	E^+	30	55.915	55.799	$(0)^u$	$1.1{\cdot}10^{-5}$	$6.6{\cdot}10^{-5}$	$5.3{\cdot}10^{-4}$	$12.6{\cdot}10^{-4}$	0.045	0.045	0.014
2	0	A_1^+	0	–	58.766	$(0)^l$	–	–	–	–	–	–	–
2	0	A_2^-	60	59.620	59.490	$(0)^u$	$9.9{\cdot}10^{-6}$	$5.4{\cdot}10^{-6}$	$6.2{\cdot}10^{-4}$	$3.9{\cdot}10^{-4}$	0.085	0.084	0.027
3	**3**	**A_2^-**	**84**	**85.068**	**84.963**	$(0)^l$	$5.4{\cdot}10^{-8}$	$2.9{\cdot}10^{-8}$	$2.2{\cdot}10^{-5}$	$1.4{\cdot}10^{-5}$	0.074	0.073	0.033
3	3	A_2^+	84	85.865	85.718	$(0)^u$	$4.5{\cdot}10^{-8}$	$2.5{\cdot}10^{-8}$	$2.0{\cdot}10^{-5}$	$1.3{\cdot}10^{-5}$	0.072	0.072	0.033
3	2	E^+	42	103.628	103.459	$(0)^l$	$4.7{\cdot}10^{-10}$	$28.0{\cdot}10^{-10}$	$7.7{\cdot}10^{-7}$	$18.4{\cdot}10^{-7}$	0.026	0.026	0.015
3	2	E^-	42	104.389	104.182	$(0)^u$	$4.0{\cdot}10^{-10}$	$23.7{\cdot}10^{-10}$	$6.9{\cdot}10^{-7}$	$16.5{\cdot}10^{-7}$	0.026	0.026	0.015
3	1	E^-	42	114.742	114.535	$(0)^l$	$4.2{\cdot}10^{-11}$	$24.9{\cdot}10^{-11}$	$1.6{\cdot}10^{-7}$	$3.7{\cdot}10^{-7}$	0.021	0.021	0.014
3	1	E^+	42	115.484	115.239	$(0)^u$	$3.6{\cdot}10^{-11}$	$21.1{\cdot}10^{-11}$	$1.4{\cdot}10^{-7}$	$3.3{\cdot}10^{-7}$	0.021	0.021	0.014
3	0	A_2^+	84	118.445	118.223	$(0)^l$	$3.7{\cdot}10^{-11}$	$2.0{\cdot}10^{-11}$	$1.8{\cdot}10^{-7}$	$1.2{\cdot}10^{-7}$	0.039	0.039	0.028
3	0	A_1^-	0	–	118.921	$(0)^u$	–	–	–	–	–	–	–
4	4	E^+	54	138.564	138.374	$(0)^l$	$3.0{\cdot}10^{-13}$	$17.8{\cdot}10^{-13}$	$6.5{\cdot}10^{-9}$	$15.5{\cdot}10^{-9}$	0.017	0.017	0.017
4	4	E^-	54	139.369	139.138	$(0)^u$	$2.5{\cdot}10^{-13}$	$14.9{\cdot}10^{-13}$	$5.8{\cdot}10^{-9}$	$13.8{\cdot}10^{-9}$	0.017	0.017	0.016
4	3	A_2^-	108	164.538	164.257	$(0)^l$	$2.1{\cdot}10^{-15}$	$1.1{\cdot}10^{-15}$	$3.1{\cdot}10^{-10}$	$2.0{\cdot}10^{-10}$	0.021	0.021	0.029
4	3	A_2^+	108	165.295	164.976	$(0)^u$	$17.6{\cdot}10^{-16}$	$9.6{\cdot}10^{-16}$	$2.8{\cdot}10^{-10}$	$1.8{\cdot}10^{-10}$	0.021	0.021	0.029
4	2	E^+	54	183.035	182.692	$(0)^l$	$1.8{\cdot}10^{-17}$	$10.9{\cdot}10^{-17}$	$1.1{\cdot}10^{-11}$	$2.6{\cdot}10^{-11}$	0.008	0.008	0.013
4	2	E^-	54	183.759	183.380	$(0)^u$	$1.6{\cdot}10^{-17}$	$9.3{\cdot}10^{-17}$	$9.8{\cdot}10^{-12}$	$23.2{\cdot}10^{-12}$	0.007	0.008	0.013
4	1	E^-	54	194.112	193.731	$(0)^l$	$1.6{\cdot}10^{-18}$	$9.8{\cdot}10^{-18}$	$2.2{\cdot}10^{-12}$	$5.2{\cdot}10^{-12}$	0.006	0.006	0.013
4	1	E^+	54	194.817	194.401	$(0)^u$	$1.4{\cdot}10^{-18}$	$8.4{\cdot}10^{-18}$	$2.0{\cdot}10^{-12}$	$4.7{\cdot}10^{-12}$	0.006	0.006	0.013
4	0	A_1^+	0	–	197.407	$(0)^l$	–	–	–	–	–	–	–
4	0	A_2^-	108	198.501	198.072	$(0)^u$	$12.7{\cdot}10^{-19}$	$6.9{\cdot}10^{-19}$	$2.3{\cdot}10^{-12}$	$1.5{\cdot}10^{-12}$	0.011	0.011	0.025
				(The final states of the measured transitions in Table 6 are given below.)									
0	0	A_2^-	12	3336.304	3336.365	$(1)^u$	0.000	0.000	0.000	0.000	$4.3{\cdot}10^{-29}$	$4.3{\cdot}10^{-29}$	$6.5{\cdot}10^{-10}$
1	1	E^-	18	3351.344	3350.812	$(1)^l$	0.000	0.000	0.000	0.000	$4.9{\cdot}10^{-29}$	$4.9{\cdot}10^{-29}$	$9.1{\cdot}10^{-10}$
1	1	E^+	18	3352.334	3351.672	$(1)^u$	0.000	0.000	0.000	0.000	$4.8{\cdot}10^{-29}$	$4.8{\cdot}10^{-29}$	$9.0{\cdot}10^{-10}$
1	0	A_2^+	36	3355.004	3355.366	$(1)^l$	0.000	0.000	0.000	0.000	$9.2{\cdot}10^{-29}$	$9.2{\cdot}10^{-29}$	$1.8{\cdot}10^{-9}$
2	2	E^-	30	3380.718	3380.088	$(1)^u$	0.000	0.000	0.000	0.000	$4.7{\cdot}10^{-29}$	$4.8{\cdot}10^{-29}$	$1.3{\cdot}10^{-9}$
2	1	E^+	30	3391.704	3391.169	$(1)^u$	0.000	0.000	0.000	0.000	$3.9{\cdot}10^{-29}$	$3.9{\cdot}10^{-29}$	$1.2{\cdot}10^{-9}$
2	0	A_2^-	60	3395.361	3394.861	$(1)^u$	0.000	0.000	0.000	0.000	$7.2{\cdot}10^{-29}$	$7.2{\cdot}10^{-29}$	$2.4{\cdot}10^{-9}$
3	3	A_2^-	84	3421.459	3420.855	$(1)^l$	0.000	0.000	0.000	0.000	$6.2{\cdot}10^{-29}$	$6.2{\cdot}10^{-29}$	$3.0{\cdot}10^{-9}$
3	2	E^-	42	3439.767	3439.321	$(1)^u$	0.000	0.000	0.000	0.000	$2.2{\cdot}10^{-29}$	$2.2{\cdot}10^{-29}$	$1.4{\cdot}10^{-9}$
3	1	E^+	42	3450.743	3450.393	$(1)^u$	0.000	0.000	0.000	0.000	$1.8{\cdot}10^{-29}$	$1.8{\cdot}10^{-29}$	$1.3{\cdot}10^{-9}$
				$\sum p$:			1.00	1.00	1.00	1.00	0.96	0.96	0.45
				$\sum Q^{rot,ns}$(v):			13.7	45.8	18.2	49.5	232.9	271.8	1666.9

Notes: The rotational quantum numbers J, K, the motional symmetry Γ_m, the degeneracy $g = g(J,K,v)$ from Equation (5), the energy above the ground state E^a and E^b, the vibrational-tunnelling state v, and at the bottom the sum $\sum p$ of the populations for E smaller than 200(hc) cm^{-1} and the sum $\sum Q^{rot,ns}(v)$ over the four vibrational-tunnelling states $(0)^{l,u}$, $(0,1,0,0)^{l,u}$ are given. The state energies E^a are taken from the MARVEL database [74] based on experimentally known levels. The state energies E^b are the calculated energies from Ref. [41] including also the symmetry forbidden states with $g = 0$. All initial states probed in the experiments are marked by bold letters and all final states of the measured transitions are given at the bottom of the table ($v = (1,0,0,0)^{u,l}$ abbreviated here as $(1)^{u,l}$). The largest population difference between nr and nc is at temperatures below 10 K with a factor of about 6 for some levels, decreasing with higher temperatures to < 0.1% difference at 296 K.

relaxation is specified as 'nr' and **c**onservation as 'nc'). The population for a state with motional symmetry Γ_m (= A or E symmetry), for the case of nuclear spin symmetry conservation after the jet expansion, is calculated according to the procedure of [28,32,36,39]. Nuclear spin symmetry conservation is fulfilled when the initial mole fraction at 296 K of the summed populations of all A-symmetric and E-symmetric states is the same before and after the jet expansion, i.e. if the two symmetries can be understood as two separate species, relaxing independently with no interconversion during the jet expansion towards the two separate ground states ($J = K = 1, \Gamma_m = E^-$ and $J = K = 0, \Gamma_m = A_2^-$ in Table 5). The mole fraction $x(\Gamma_m^s; T)$ at thermal equilibrium of Γ_m^s (of all states with motional symmetry Γ_m) is calculated by

$$x(\Gamma_m^s; T) = Q(\Gamma_m^s; T) \cdot \exp\left[-E_0(\Gamma_m^s)/(kT)\right] / Q_{nr}(T) \quad (7)$$

Table 6. Measured transition wavenumbers $\tilde{\nu}_0$ with uncertainty estimate $\Delta\nu$ from Equation (22) and deviation from the values listed in the HITRAN $\nu_{\mathrm{H.}}$ [73] and MARVEL databases $\nu_{\mathrm{M.}}$ [74].

	J''	K''	Γ'' $(S)_3^*$	J'	K'	Γ' $(S)_3^*$	$\tilde{\nu}_0$/cm^{-1}	$\Delta\nu$/MHz	$(\nu-\nu_{\mathrm{H.}})$/MHz	$(\nu-\nu_{\mathrm{M.}})$/MHz	$(\tilde{\nu}-\tilde{\nu}_{\mathrm{A.}})$/cm^{-1}	mix. ID
R(0,0,*u*)							3355.00728	0.5	193.6	105.56	−0.36	1
R(0,0,*u*)	0	0	A_2^-	1	0	A_2^+	3355.00723	0.5	192.2	104.09	−0.36	5
R(0,0,*u*)							3355.00725	0.4	192.7	104.58	−0.36	12
Q(1,1,*l*)				1	1	E^+	3336.95157	0.6	−0.4	−4.75	−0.08	3
R(1,1,*l*)	1	1	E^-				3376.32580	0.5	0.3	−2.50	−0.20	3
R(1,1,*l*)				2	1	E^+	3376.32582	0.5	0.8	−1.96	−0.20	12
Q(1,1,*u*)	1	1	E^+	1	1	E^-	3335.17135	0.4	5.4	−0.38	−0.25	4
R(1,0,*l*)				2	0	A_2^-	3376.26979	1.7	5.3	161.69	0.49	1
R(1,0,*l*)	1	0	A_2^+				3376.26964	1.0	1.0	157.39	0.49	3
R(1,0,*l*)							3376.26957	3.1	−1.1	155.29	0.49	12
P(1,0,*l*)				0	0	A_2^-	3317.20725	2.2	6.8	6.27	−0.07	4
P(1,0,*l*)							3317.20722	0.5	5.9	5.35	−0.07	6
P(1,0,*l*)							3317.20730	0.5	8.5	7.97	−0.07	7
R(2,2,*l*)				3	2	E^-	3395.76457	0.9	−8.3	−12.45	−0.34	9
Q(2,2,*l*)	2	2	E^+				3336.71584	0.5	−0.5	−5.13	−0.16	2
Q(2,2,*l*)				2	2	E^-	3336.71596	0.5	2.9	−1.72	−0.16	11
R(2,1,*l*)				3	1	E^+	3395.59851	2.0	−0.9	−5.93	−0.48	9
Q(2,1,*l*)	2	1	E^-				3336.55985	5.0	−6.6	−8.78	−0.29	2
Q(2,1,*l*)				2	1	E^+	3336.56022	2.0	4.4	2.22	−0.29	8
Q(2,1,*l*)							3336.56019	2.8	3.6	1.48	−0.29	11
Q(3,3,*l*)	3	3	A_2^-	3	3	A_2^+	3336.39017	1.1	−12.1	−8.01	−0.25	10

Notes: The results are compared to the rovibrational calculations $\nu_{\mathrm{A.}}$ from Ref. [41] using the AMMPOT4 potential from Ref. [72]. Mixtures as given by ID in Table 1.

where $Q_{nr}(T)$ is the complete relaxed partition function with the ground state ($J = K = 0, A_2^-$) (including rotation, vibration, tunnelling and nuclear spin) and $Q(\Gamma_m^s; T)$ is the partition function including only states with symmetry A or E referenced to the lowest energy $E_0(\Gamma_m^s)$ of this symmetry with distinction of only A and E in Γ_m^s, as interconversion between levels of different parity in NH_3 is considered to be frequent in collisions (although total parity including the collision partner is conserved [1,2])

$$Q_{nr}(T) = \sum_{\Gamma_m^s} Q(\Gamma_m^s; T) \exp\left[-E_0(\Gamma_m^s)/(kT)\right] \quad (8a)$$

$$Q(\Gamma_m^s; T) = \sum_{\forall (J,K,\mathbf{v}) \text{ with } \Gamma_m^{(J,K,\mathbf{v})}=\Gamma_m^s} g(J,K,\mathbf{v}) \cdot \exp\left[-(E_{J,K,\mathbf{v}} - E_0(\Gamma_m^s))/(kT)\right] \quad (8b)$$

and

$$E_0(\Gamma_m^s) = \begin{cases} E^u_{0,0,(0)}, & \text{if } \Gamma_m^s = A \\ E^l_{1,1,(0)}, & \text{if } \Gamma_m^s = E \end{cases} \quad (9)$$

With this, we have for the case of total nuclear spin symmetry relaxation for the population of a state $(J, K, \mathbf{v})$ at the temperature T

$$p_{nr}(J,K,\mathbf{v};T) = g(J,K,\mathbf{v}) \cdot \exp\left[-E_{(J,K,\mathbf{v})}/(kT)\right]/Q_{nr}(T) \quad (10)$$

and for total nuclear spin symmetry conservation we have

$$p_{nc}(J,K,\mathbf{v};T_{rot}) = x(\Gamma_m^s; T_{init}) \cdot g(J,K,\mathbf{v}) \cdot \exp\left[-\left(E_{J,K,\mathbf{v}} - E_0(\Gamma_m^s)\right)/(kT_{rot})\right]/Q(\Gamma_m^s; T_{rot}) \quad (11)$$

where T_{rot} is the effective rotational temperature of the vibrational ground state in the jet expansion, and the initial temperature $T_{init} = T_{room} = 296\,K$ is used for the mole fraction before the expansion, assuming no symmetry specific trapping in excited vibrational states. This would in any case contribute only a very minor fraction.

Thermal equilibrium can be assumed for the NH_3 samples used in the experiment before expansion. For the calculation of $x(\Gamma_m^s; T_{room})$ only the two vibrational-tunnelling ground states and the two lowest excited vibrational-tunnelling levels of the symmetric bending (inversion) vibration ν_2 are included. However all possible rotational states of these four vibrational-tunnelling states up to $J \leq 20$ ($\approx 5000\,cm^{-1}$ total energy) are used, i.e. the sum in Equation (8b) includes only these four vibrational-tunnelling states. The populations of higher vibrational-tunnelling states are much below 1% (see Table 4) and are neglected except for comparison with the total partition functions. In the following calculations, the state energies from the HITRAN and MARVEL databases are used [73,74]. These agree for the states considered to within better than $10^{-3}(hc)\,cm^{-1}$ except for the six states ($J = 2, K = 2, E^+, (0,0,0,0)^l$), ($J = 3, K = 2, E^-, (0,0,0,0)^u$), ($J = 3, K = 1, E^+, (0,0,0,0)^u$), ($J = 4, K = 2, E^+, (0,0,0,0)^l$), ($J = 4, K = 4, E^+, (0,1,0,0)^u$)

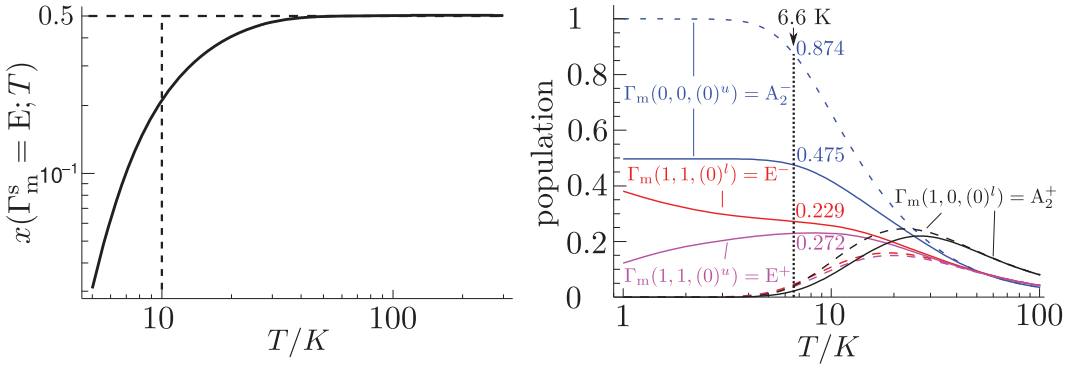

Figure 11. *Left*: Mole fraction $x(\Gamma_m^s = E; T)$ of the E-symmetry states of NH_3 in the temperature range from 5 K to 300 K (logarithmic scale) assuming equilibrium, i.e. for total relaxation, at room temperature $x(\Gamma_m^s = E; T = 296\,K) = 0.5028$ and at a jet expansion temperature $x(\Gamma_m^s = E; T = 6.6\,K) = 0.0848$. *Right*: Population of the lowest four states in the temperature range from 1 K to 100 K. The dashed lines are for assumed total relaxation and the solid lines are for complete nuclear spin symmetry conservation. The corresponding lines almost coincide above 30 K and differ strongly below 10 K. Some populations are given explicitly at the temperature of 6.6 K, corresponding to the rotational temperature obtained for $H = 5.1(2)$ mm as the distance between the centre axis of the laser cavity mode and the slit exit.

and $(J = 4, K = 4, E^-, (0,1,0,0)^l)$, all of which differ by less than $2 \cdot 10^{-3}(hc)\,cm^{-1}$. This is negligible for all of the following calculations. At 296 K, the E- and A-symmetry states are essentially equally populated with the mole fraction $x(\Gamma_m^s = E; T_{room}) = 0.5028$. This is effectively consistent with the classical high temperature limit of 0.5, which follows from the regular property of the classical density of states, i.e. [1,2,78]

$$N_c(\Gamma) = [\Gamma] \Big/ \sum_k [\Gamma_k] \tag{12}$$

Here $N_c(\Gamma)$ is the ratio between the number of states with symmetry Γ and the total number of states with the dimension of the symmetry species $[\Gamma_k] = 2$ for E and $[\Gamma_k] = 1$ for A. Including the nuclear spin weights shows that the mole fraction in the classical high temperature limit is $x_c(A) = x_c(E) = 0.5$. As the more abundant species in this limit is by convention called ortho and the less abundant para species, there is, strictly speaking, no ortho–para convention for NH_3. Therefore, we simply call these nuclear spin isomers the A and E isomers. Sometimes the species with the higher nuclear spin weight is called ortho, which is, however, not consistent with the general convention. Figure 11 shows $x(\Gamma_m^s = E; T)$ for the range between 5 K and 300 K assuming complete nuclear spin symmetry relaxation (nr). The high temperature limit is already closely approached at 30 K. Table 5 provides also an overview of the expected populations after the jet expansion with assumed total nuclear spin relaxation using Equation (10) and with total nuclear spin conservation using Equation (11).

The populations of the vibrational levels below $3500\,cm^{-1}$ at 296 K are listed in Table 4. We distinguish between each vibrational level and between the inversion tunnelling sublevels, resulting in 22 different vibrational-tunnelling levels. This sums up to the practically converged vibrational-tunnelling partition function $Q_{vib.tun.} = 2.026$ at 296 K (see also [72] for vibrational excitations above $3500\,cm^{-1}$). Different approximations can be used for the partition functions. For the four lowest vibrational-tunnelling levels including the ground state and the inversion fundamental ν_2, all relevant rotational levels with $J \le 20$ are tabulated in [74] based on experimental data. The exact summation leads to $Q_{nr}(T = 296\,K) = [Q_{nr}^{rot,ns}((0,0,0,0)^l) + Q_{nr}^{rot,ns}((0,0,0,0)^u) + Q_{nr}^{rot,ns}((0,1,0,0)^l) + Q_{nr}^{rot,ns}((0,1,0,0)^u)] = 1666.921$. Here we have grouped the complete partition function into the contributions from each vibrational-tunnelling state

$$Q_{nr}^{rot,ns}(\mathbf{v}_i) = \sum_{\forall J \le 20, K} g(J,K,\mathbf{v}_i) \cdot \exp\left[-E_{(J,K,\mathbf{v}_i)}/(kT)\right] \tag{13}$$

This is, however, not quite converged as far as higher vibrationally excited states are concerned. These are weakly populated at 296 K. Using various approximations including more highly excited states, one obtains values for $Q_{nr}(T = 296\,K)$ in the range of about 1700–1730, as also given in Ref. [79] (1725.2), Ref. [80] (1731.5), and Ref. [81] (1725.24). The differences are irrelevant for our analysis. At the lower temperatures, which are of importance for our experiments, the direct summation including the experimentally known levels from [74] with $J \le 20$, using the lowest four vibrational-tunnelling levels, can be considered as converged (see also Table 5 for the populations).

For the results in Section 4, we report rovibrational transitions for the A_1 symmetric stretching fundamental

ν_1 ($(0)^{l,u} \rightarrow (1)^{l,u}$) centred near 3340 cm^{-1}. The selection rule for this parallel band is $\Delta K = 0$. The absolute line strengths as integrated cross section $G_{f\,i}$ is given by [82,83]

$$G_{f\,i} = \int \sigma_{f\,i}(\tilde{\nu})\tilde{\nu}^{-1}d\tilde{\nu} = 1/(C_i l)\int_{line} \ln(I_0/I)\tilde{\nu}^{-1}d\tilde{\nu} \tag{14}$$

$\sigma_{f\,i}(\tilde{\nu})$ is the absorption cross section for the transition $i \rightarrow f$, C_i is the concentration of the lower state i (as particle density), and C_f as the concentration of the upper state being negligible (see Table 5). For the electric dipole transitions considered here, we have the practical equation [82]

$$G_{f\,i}/pm^2 \approx 41.624\ |M_{f\,i}/D|^2 \tag{15}$$

with $M_{f\,i}$ the electric dipole transition moment (and with the electric dipole operator $\hat{\mu}_{el}$)

$$M_{f\,i} = \langle f|\hat{\mu}_{el}|i\rangle \tag{16}$$

To a good approximation, one has the commonly used line strength $S_{f\,i}$

$$S_{f\,i} = 1/(C_i l)\int_{line} \ln(I_0/I)d\tilde{\nu} \approx \tilde{\nu}_0 \cdot G_{f\,i} \tag{17}$$

with the line centre $\tilde{\nu}_0$. Comparing with Equation (3) ($\alpha' = \sigma_{f\,i} \cdot C_i$) we obtain, with the approximation $\ln(1+x) \approx x$ for small absorbances,

$$S_{f\,i} = 1/(C_i l)\int_{line} \ln\left[I_0/\left(I_0 \cdot (1 - A_{pp})\right)\right] d\tilde{\nu} \simeq 1/(C_i l) \times \int A_{pp} d\tilde{\nu} = \bar{A}_{f\,i}/(C_i l) \tag{18}$$

We note that in a jet expansion the concentration C_i is not position independent, C_i and l are thus nominal values, but one can derive an effective average concentration over the total length L or L_{Slit} in the cavity with equivalent results concerning the absorption. For the analysis of relative populations, one can to a good approximation use the line strengths [83] from the Hönl–London approximation [39,71]:

$$G_{K_i J_i} = a \cdot A_{K_i J_i} \cdot g(J, K, \mathbf{v}) \cdot \exp\left[-E_{K_i J_i}/(kT_{rot})\right] \tag{19}$$

Here a is a constant independent of K_i and J_i and proportional to the absolute square of the vibrational electric dipole transition moment, $g(J, K, \mathbf{v})$ the degeneracy factor from Equation (5), and $A_{K_i J_i}$ the Hönl–London factor. One can test the validity of this approximation for the transitions considered by comparison with accurate theoretical line strengths [41] and with results from [73] (see Table 8 in results section 4.3). For relative populations of different initial states i and j, to be determined in our experiments, we thus have ($S_{f\,i} \propto p_i \cdot A_{K_i J_i}$):

$$p_i/p_j \approx \frac{S_{f\,i} A_{K_j J_j}}{S_{f\,j} A_{K_i J_i}} \approx \frac{\bar{A}_{f\,i} A_{K_j J_j}}{\bar{A}_{f\,j} A_{K_i J_i}} \tag{20}$$

In our experiment, we generally obtain a good fit of a Gaussian (Doppler) line profile to the experimental

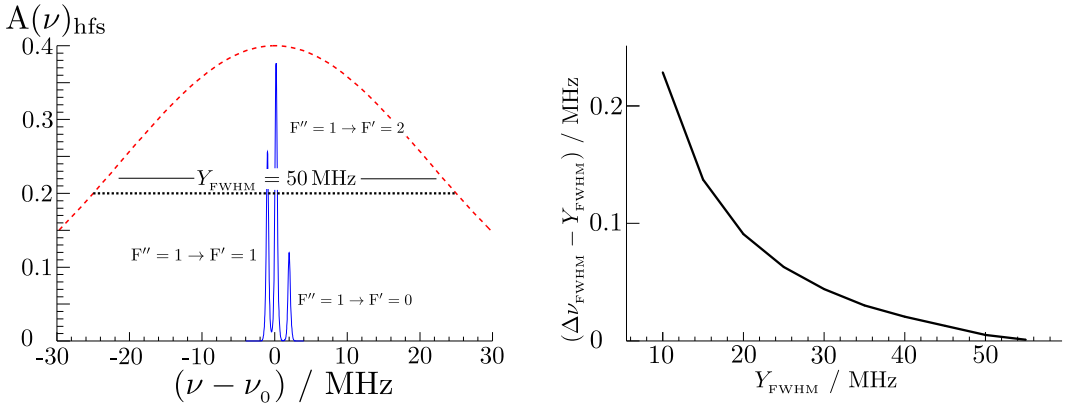

Figure 12. *Left*: The calculated absorption signal $A(\nu)_{hfs}$ including the hyperfine splitting and power broadening is presented with $\vec{F}$, the total angular momentum ($\vec{F} = \vec{J} + \vec{I}$). The hyperfine structure from the protons is much smaller and neglected here. The calculation used Equations (20) and (21) from Ref. [46] for the transition R(0,0,*u*). As a comparison, a Gaussian with a $Y_{FWHM} = 50$ MHz corresponding to the experimental width is drawn (red dashed line). *Right*: The additional broadening is presented when the hyperfine splitting and power broadening are included. For this calculation, the expected absorption $A(\nu)_{hfs}$ is convoluted with Gaussians with a width of Y_{FWHM}. The resulting Gaussian-like function was fitted with a new Gaussian giving $\Delta\nu_{FWHM}$ resulting in the expected additional width $\Delta\nu_{FWHM} - Y_{FWHM}$ from a measured function compared to the initial ideal Gaussian with width Y_{FWHM}. The effect is only in the order of 10 kHz for the experimental resolution of 50 MHz.

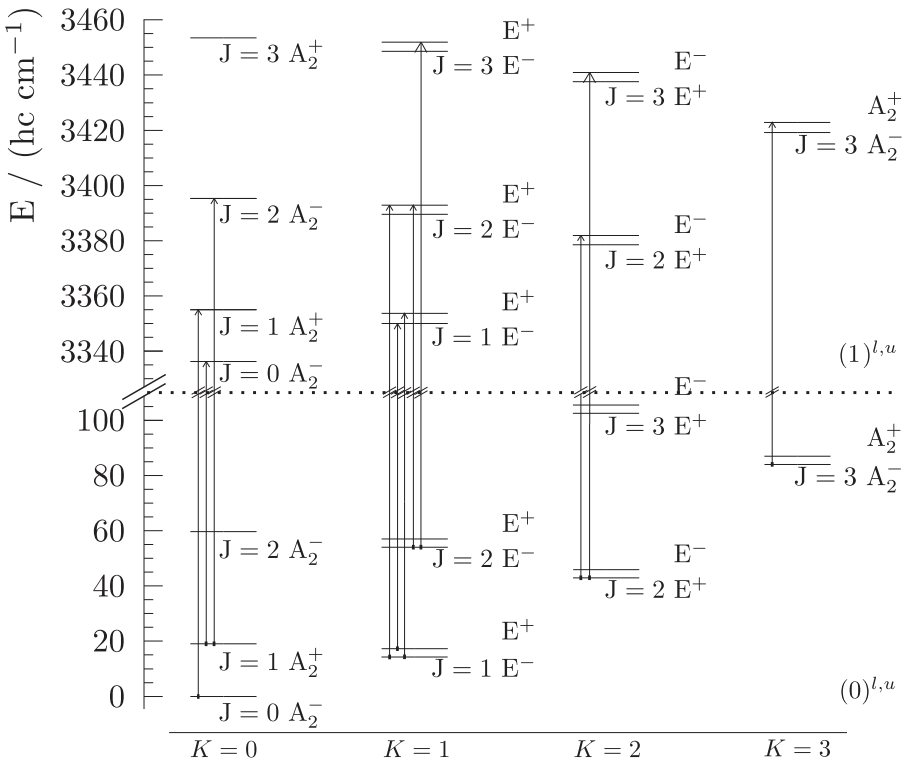

Figure 13. Overview of the measured parallel band transitions ($\Delta K = 0$) from the vibrational ground state to the first excited state of the symmetric NH-stretching vibration ν_1. The tunnelling splittings are enlarged by a factor 3 for better visibility. The motional symmetry Γ_m is given for each state. A complete list of all measured transitions is given in Table 6.

absorbances as a function of frequency

$$A(\nu) = A_{BG} + A_{max} \cdot \exp\left[-4\ln 2\left(\frac{\nu - \nu_0}{\Delta\nu_{FWHM}}\right)^2\right] \quad (21)$$

ν is the actual frequency, A_{BG} is a small background from residual gas of the previous gas jet pulses, A_{max} is the scaling for the amount of absorbance, ν_0 is the position of the molecular transition and $\Delta\nu_{FWHM}$ is the full width at half maximum. We have estimated theoretically the effects of power broadening and hyperfine structure (see figure 12 and appendix) and found them to be negligible because of the large Doppler widths of about $\Delta\nu_{FWHM} =$ 60 MHz under our experimental conditions. For this estimate, the hyperfine splitting and power broadening for one transition was calculated numerically (following [46, Section III. B.]) with the maximum possible internal cavity ring-down intensity of 1 kW/cm^2 resulting in a calculated theoretical absorption signal $A(\nu)_{hfs}$. This signal was then convoluted with Gauss functions of different widths, simulating the effect of Doppler broadening. Subsequently, these convolutions were each fitted with the Gauss function from Equation (21) (to mimic the applied fit to the experimental lines). Figure 12 shows a simulation of a spectrum including hyperfine structure (as measured in [46] and calculated from the parameters in the appendix). The effect on the observed Doppler line shape is small and negligible for all of our measurements (see also discussion in the results, Section 4).

4. Results

4.1. Transition frequency measurements

Figure 13 and Table 6 provide a survey of all measured lines together with the relevant notations. Since all measured transitions have an initial state $(J, K, i) = (J, K, (0, 0, 0, 0)^i)$ from the vibrational ground state, we use R(J'',K'',i) for a transition with $\Delta J = J' - J'' = +1$, Q(J'',K'',i) for $\Delta J = 0$, and P(J'',K'',i) for $\Delta J = -1$ with the lower state given in parentheses ($i = \{u, l\}$ see above). We fit the Gaussian line shape function from Equation (21) to the absorbance, providing as a mean value the measured transition frequency. The uncertainty can be estimated from the differences in independent measurements with different gas mixtures of the same transition listed in Table 6. Estimating the uncertainty of the absorbance only by the statistical fluctuation of the cavity ring-down times underestimates the uncertainty for small signals ($A_{pp} < 10^{-4}$), which are more vulnerable to small changes of the setup between

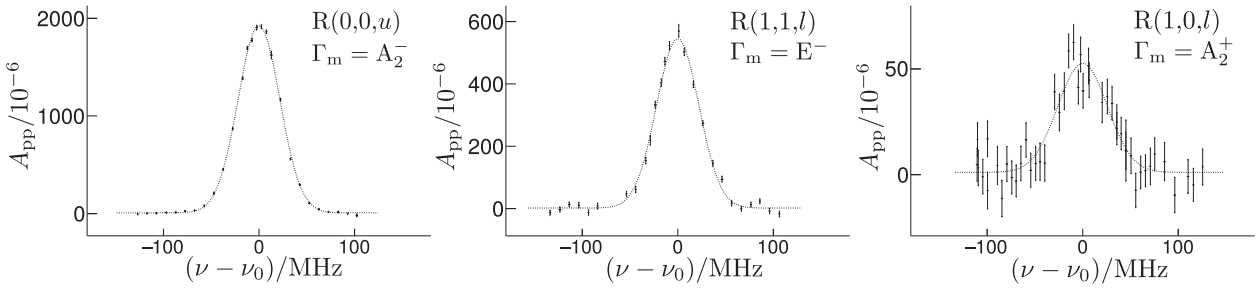

Figure 14. Measured spectra of the transitions R(0,0,*u*) with $\tilde{\nu}_0 = 3355.00725(1)(hc)\,\mathrm{cm}^{-1}$ (left), R(1,1,*l*) with $\tilde{\nu}_0 = 3376.32582(2)\,\mathrm{cm}^{-1}$ (middle), and R(1,0,*l*) with $\tilde{\nu}_0 = 3376.26957(10)\,\mathrm{cm}^{-1}$ (right), with $\nu_0 = c \cdot \tilde{\nu}_0$ and with the uncertainty estimation from Equation (22) in parentheses. All three spectral lines are measured with an identical setup ($H = 5.1(2)$ mm, mixture ID = 12 with $x(\mathrm{NH_3}) = 0.000100(2)$). The ratio of the line strengths between R(0,0,*u*) and R(1,0,*l*) results in the effective rotational temperature of 6.6(1) K (independent of the two assumptions of nuclear spin conservation or relaxation) and the ratio of R(1,1,*l*) and R(1,0,*l*) is consistent with nuclear spin symmetry conservation and the same effective rotational temperature 6.64(9) K, while nuclear spin symmetry relaxation would result in an inconsistent value of 1.68(3) K. The Doppler widths are for R(0,0,*u*) $\Delta\nu_{\mathrm{FWHM}} = 51.5(3)$ MHz, for R(1,1,*l*) $\Delta\nu_{\mathrm{FWHM}} = 52.2(8)$ MHz, and for R(1,0,*l*) $\Delta\nu_{\mathrm{FWHM}} = 61.1(49)$ MHz corresponding to apparent translational 'temperatures' of 8.7(1) K, 8.8(3) K, and 12.1(19) K.

Table 7. Comparison of R(0,0,*u*) and R(1,0,*l*) transition wavenumbers with previous experimental results from the literature.

Ref.	Year		*T*/K	R(0,0,*u*), $\tilde{\nu}_0$/(cm^{-1})	$\Delta\nu$/(MHz)	R(1,0,*l*), $\tilde{\nu}_0$/(cm^{-1})	$\Delta\nu$/(MHz)
(this work)		supers. jet exp.	< 8	3355.00725(2)	0.0	3376.26964(3)	0.0
[73]	2013	(HITRAN)		3355.00082	193.6	3376.26961	1.0
[74]	2015	(MARVEL)		3355.003758	105.6	3376.264394	157.4
[84]	1989	FTIR	room	3355.00098	188.1	3376.26959	2.3
[85]	1985	FTIR	297	3355.0057	46.6	3376.2686	32.0
[86]	1993	diff.-freq. laser spectr.	297±1	3355.00569	46.9	3376.2686	32.0
[46]	2015	supers. jet exp.	< 10	3355.00725	0.1	–	–
[87]	1999	FTIR	290–298	–	–	3376.26976	−2.8

Notes: The uncertainty estimate from Equation (22) is given in parentheses and $\Delta\nu = \nu_0 - \nu_{\mathrm{Literature}}$ is the difference to the measured value $\nu_0 = c \cdot \tilde{\nu}_0$ of our work.

different frequency points caused by e.g. gas pressure before expansion, laser cavity alignment or laboratory temperature. To account for this, the influence of fluctuations was estimated by adding noise to each sample absorbance (uniformly distributed in the interval $[-A_{\mathrm{noise}}, A_{\mathrm{noise}}]$) with the subsequent repeated Gaussian fit resulting in a new transition frequency. From the distribution of this artificially generated transition frequencies, the standard uncertainty introduced by noise $\sigma_{\mathrm{noise}}(A_{\mathrm{noise}})$ was obtained in the size of the residuals. The stated total frequency uncertainty $\Delta\nu$ in Table 6 consists then of two contributions in Equation (22)

$$\Delta\nu = \sigma_{\mathrm{fit}} + \sigma_{\mathrm{noise}}(A_{\mathrm{noise}} \approx 10^{-5}) \qquad (22)$$

This should provide an adequate estimate for the frequency uncertainty [83]. The uncertainty of the laser frequency is much smaller and can be neglected (see Section 2.2). The transition R(0,0,*u*) deviates by about 200 MHz from the HITRAN database [73], which is much more than the uncertainty in our experiment even if the uncertainty estimate from Equation (22) were considered to be somewhat optimistic. Large discrepancies (100–200 MHz) are also seen with respect to the MARVEL tables [74] with R(1,0,*l*) (see Table 6). We have also compared with the data from the original literature on which the HITRAN and MARVEL data are based, as well as further additional sources (see Table 7). As can be seen, there is a certain variation in the results. Some of the differences might be due to partial blending of lines in the room temperature spectra. Our results agree perfectly with the accurate measurements in supersonic jets as reported in [46] (including hyperfine resolution). We thus think that our results provide accurate transition wavenumbers to within about the uncertainties given, as discussed above. With the measurement of Q(1,1,*l*) and Q(1,1,*u*), we also provide a measurement of the sum of the tunnelling splittings in the ν_1 symmetric stretching fundamental and the ground state splitting with $3336.95157(2)\,\mathrm{cm}^{-1} - 3335.17135(1)\,\mathrm{cm}^{-1} = 1.78022(3)\,\mathrm{cm}^{-1}$ with estimated uncertainty in terms of the last digit in parentheses. Subtracting the ground state splitting of $0.790365\,\mathrm{cm}^{-1}$ from [74] results in the tunnelling splitting of the ν_1 symmetric stretching fundamental for $J = 1$, $K = 1$ of $0.89855(3)\,\mathrm{cm}^{-1}$. The theoretical value from [41] for this splitting is $0.8609056\,\mathrm{cm}^{-1}$. The change from the ground state splitting is thus only minor, in contrast to many other vibrational levels in $\mathrm{NH_3}$ [41] and also

Table 8. Overview about the measured ratios of populations between two different initial states.

						T_{rot}/K			
		$\Gamma_{m,i}/\Gamma_{m,j}$	H/mm	$x(NH_3)$	p_i/p_j	nr	nc	S_{ik}/S_{jn}	$A_{K_iJ_i}/A_{K_jJ_j}$
1:	R(0,0,*u*) / R(1,0,*l*)	A/A	5.1(2)	0.000100(2)	22.2(36)	6.6(1)		1.41	1.49
2:	R(1,1,*l*) / R(1,0,*l*)	E/A			12.0(22)	1.68(3)	6.64(9)	0.75	0.75
3:	R(0,0,*u*) / R(1,1,*l*)	A/E			1.9(1)	22.92(31)	5.58(1.62)	1.88	1.99
1*:	R(0,0,*u*) / R(1,0,*l*)	A/A	3-4	0.0007(2)	8.8(7)	8.6(1)		1.41	1.49
5*:	Q(2,2,*l*) / Q(2,1,*u*)	E/E		0.015(1)	5.3(4)	9.6(1)		4.00	4.00
2*:	R(1,1,*l*) / R(1,0,*l*)	E/A		0.00010(2)	5.7(4)	2.20(2)	8.17(5)	0.75	0.75
4*:	Q(1,1,*l*) / P(1,0,*l*)	E/A		0.0012(3)	3.6(3)	2.09(3)	9.01(9)	1.55	1.51
6*:	R(2,2,*l*) / R(2,1,*u*)	E/E		0.022(3)	2.8(2)	15.6(4)		0.62	0.63
5:	Q(2,2,*l*) / Q(2,1,*u*)	E/E	2.6(2)	0.008(1)	2.6(2)	16.5(5)		4.00	4.00

Notes: For all ratios with mixed symmetry (A and E), a clear preference for nuclear spin symmetry conservation is seen. In the first column, the labels from Figure 17 are given. 'p_i/p_j' is the ratio of the obtained line intensity ratios divided by the ratio of the Hönl–London factors ($A_{K_iJ_i}/A_{K_jJ_j}$). S_{ik}/S_{jn} gives the line intensity ratio as stated in [73]. T_{rot} gives the corresponding effective rotational temperature for each measured ratio 'p_i/p_j' with assumed nuclear spin symmetry relaxation 'nr' and with nuclear spin symmetry conservation 'nc'. In the measurements with $H = 3$ to 4 mm, the distance 'H' between the centre of the cavity laser mode and the slit nozzle exit can only be restricted to a range of 3–4 mm. In the other measurements, the distance was carefully obtained with a knife edge measurement. For a higher concentration ($x(NH_3) > 0.02$) and for $H < 3$ mm, the rotational temperature is increased.

very different for ν_1 in ND_3, where the tunnelling splitting increases by a factor of 10 with excitation of the symmetric stretching vibration [69]. From P(1,0,*l*), one obtains by adding the rotational term value in the ground state a direct measurement for the lowest Pauli-allowed term value ($J = K = 0, A_2^-$) of ν_1 ($(1,0,0,0)^u$) as $\tilde{\nu} = 3336.30374(\pm 0.00007)\ \mathrm{cm}^{-1}$, where the uncertainty estimate is given for the three independent measurements and a Student t-distribution at 95% confidence.

4.2. Number density estimation

The concentration C of NH_3 molecules as particle number density at the position of the laser cavity mode can be estimated for the measured i to f transition from Equations (18) and (20) with

$$C \approx \frac{\bar{A}_{fi}}{L_{\mathrm{Slit}} \cdot S_{fi} \cdot p_i(T_{\mathrm{rot}})/p_i(300\ \mathrm{K})} \tag{23}$$

with $L_{\mathrm{Slit}} = 40$ mm the length of the slit nozzle, p_i the population of the initial state, $\bar{A}_{fi}$ the integrated attenuation per pass, and S_{fi} the line strength for the transition at room temperature given in Ref. [73]. Using the results for $H = 5.1(2)$ mm (see Section 4.3, Figure 14) with a rotational temperature of 6.6 K gives a concentration of about $C_{NH_3} = N_A \cdot 3 \cdot 10^{-6}\ \mathrm{mol/m^3}$. Dividing by the initial mole fraction of NH_3 for this measurement (10^{-4}) gives an estimate for the argon density of $C_{tot} \approx C_{Ar} = N_A \cdot 3 \cdot 10^{-2}\ \mathrm{mol/m^3}$. This concentration would correspond to a pressure of 0.8 mbar at room temperature. Assuming Lambert's cosine law for the expansion distribution in Θ (see Figure 5 for the definition of Θ) relates the measured peak concentration at $H = 5.1(2)$mm to the total ejected number of particles per pulse with

$$N_{tot} \approx \Delta t \cdot H \cdot L_{\mathrm{Slit}} \int_{-\pi/2}^{+\pi/2} C_{Ar}\ \nu_{Ar}\ \cos(\Theta) d(\Theta)$$
$$\approx N_A \cdot 10^{-6}\ \mathrm{mol} \tag{24}$$

with w the waist of the laser cavity mode, $\nu_{\mathrm{Ar}} = 472$ m/s the velocity of the ejected atoms, $\Delta t = 150\ \mu$s the average opening time of the slit nozzle and L_{Slit} the length of the slit nozzle. N_{tot} corresponds to a total volume of about 0.017 ml per pulse from the gas bottle before the expansion, which is similar to the upper limit from the gas consumption of about 0.020 ml including leakage (mainly through the closed slit) in the time between the gas pulses (see Section 2.4).

4.3. Rotational temperature and relative population measurements

The effective rotational temperature can be probed by comparing line intensities, which are proportional to the initial state population in different rotational states of the same nuclear spin symmetry (see Equation (20)). Measurement of line intensities in rotational states of different nuclear spin symmetry provides information about nuclear spin symmetry conservation or relaxation.

The three measurements shown in Figure 14 are used to probe the ratios between the populations of the three energetically lowest states (with $E_{0,0,u} = 0\ \mathrm{cm}^{-1}$, $E_{1,1,l} = 15.4(hc)\ \mathrm{cm}^{-1}$ and $E_{1,0,l} = 19.1(hc)\ \mathrm{cm}^{-1}$, see Table 5 and Figure 13). If the populations of the same symmetry species are compared, it is expected that no difference in the rotational temperature for the two assumptions of nuclear spin symmetry relaxation or conservation can be seen. Comparing the lines R(0,0,*u*) and

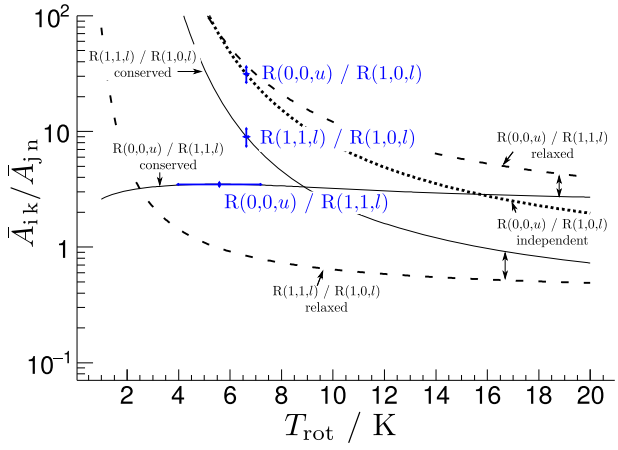

Figure 15. Measured integrated line intensity ratio $\bar{A}_{ik}/\bar{A}_{jn}$ compared to the calculated ratio from Equation (20) assuming nuclear spin symmetry relaxation using Equation (10) and conservation Equation (11) for the transitions R(0,0,*u*)/R(1,0,*l*), R(1,1,*l*)/ R(1,0,*l*) and R(0,0,*u*)/R(1,1,*l*) from Figure 14. The calculated lines give the temperature dependence for each intensity ratio. The ratio of line intensities for the same nuclear spin symmetry (R(0,0,*u*)/R(1,0,*l*)) is independent of the relaxation model (shown by a dotted line). Ratios of line intensities for different nuclear spin symmetries (R(1,1,*l*)/ R(1,0,*l*) and R(0,0,*u*)/R(1,1,*l*)) depend on the relaxation model and are shown as solid lines for nuclear spin symmetry conservation and as dashed lines for complete nuclear spin symmetry relaxation. The measured ratios $\bar{A}_{ik}/\bar{A}_{jn}$ are shown at the corresponding rotational temperature for nuclear spin symmetry conservation.

R(1,0,*l*), both with A symmetry, results in an effective rotational temperature after the jet expansion of 6.63(8) K. The comparison between R(0,0,*u*) or R(1,0,*l*) with R(1,1,*l*), which has E symmetry, with the assumption of nuclear spin symmetry conservation results in effective rotational temperatures of 5.6(1.6) K for R(0,0,*u*) and 6.64(9) K for R(1,0,*l*). These results are in good agreement for all three effective rotational temperatures, while with the assumption of nuclear spin symmetry relaxation one obtains apparent effective rotational temperatures of 22.92(31) K for R(0,0,*u*) and 1.68(3) K for R(1,0,*l*), resulting in three very different apparent effective rotational temperatures. The stated uncertainty of the effective rotational temperature given in parentheses is the standard uncertainty from the fit of the ratio of integrated line intensity $\bar{A}_{ik}/\bar{A}_{jn}$ to the expected temperature dependence from Equation (20) with the uncertainty of $\bar{A}_{ik}/\bar{A}_{jn}$ estimated by the first-order error analysis using the parameter from Equation (21), $\sigma_{A_{max,ik}}$, $\sigma_{A_{max,jn}}$, $\sigma_{\Delta\nu_{FWHM,ik}}$ and $\sigma_{\Delta\nu_{FWHM,jn}}$. The large uncertainty of the effective rotational temperature (5.6(1.6) K) for R(0,0,*u*)/R(1,1,*l*) is caused by the weak temperature dependence for this ratio, when nuclear spin symmetry conservation is assumed (see Figures 15 and 11).

In some measurements, the rotational temperature is also determined by comparing the line intensities from R(0,0,*u*) and R(1,0,*l*), for two A-symmetry states, with one gas mixture, and the line intensities from Q(2,2,*l*) and Q(2,1,*l*), for two E-symmetry states, with a different and higher mixture concentration. The weakly populated initial states (2,2,*l*) and (2,1,*l*) (with $E_{2,2,l} = 44.0(hc)\ \mathrm{cm}^{-1}$ and $E_{2,1,l} = 55.144(hc)\ \mathrm{cm}^{-1}$) could be measured with this as well.

In Figure 16, these measurements are shown, resulting in a rotational temperature of 8.55(5) K for levels with A-symmetry and of 9.6(3) K for levels with E-symmetry. The effective rotational temperature was also determined using four additional lines comparing E- and A-symmetry, (R(1,1,*l*)/R(1,0,*l*) with mixture 3 and Q(1,1,*l*)/P(1,0,*l*) with mixture 4); the expansion is tested for nuclear spin symmetry conservation, where then all four ratios lead to the same effective rotational temperature in an interval of ±0.8 K. If total nuclear spin symmetry relaxation is assumed the effective rotational temperature for the transitions comparing the different symmetries is about 2 K, which is not consistent with the independently measured effective rotational temperatures of the symmetries E or A. The measurements at the higher temperatures were affected by the NH_3 concentration and the distance *H* between the centre axis of the laser cavity mode and the slit nozzle exit influencing the effective rotational temperature of the jet. Here the distance varied between 3 and 4 mm due to laser cavity realignment. To investigate the dependence on *H* the effective rotational temperature was also measured at a distance of $H = 2.6(2)$ mm and at $H = 5.1(2)$ mm.

At a distance of $H = 2.6(2)$ mm, a higher effective rotational temperature of 16.5(5) K and at $H = 5.1(2)$ mm a lower effective rotational temperature of 6.6(1) K was obtained. A list of all additional effective rotational temperatures is given in Table 8 and Figure 17. While the results at the higher temperatures have larger systematic uncertainty, than the results at 6.6 K, they are also consistent with nuclear spin symmetry conservation and inconsistent with the assumption of complete nuclear spin symmetry relaxation. They provide in addition evidence for a common effective rotational temperature for several different rotational levels, not just two. A survey of all measured lines is given in the appendix.

5. Discussion and conclusion

We have presented here a new experimental setup for measuring high-resolution mid-IR spectra of polyatomic molecules by means of a combination of an optical parametric oscillator (OPO) referenced to a frequency comb with a supersonic jet expansion from a pulsed slit

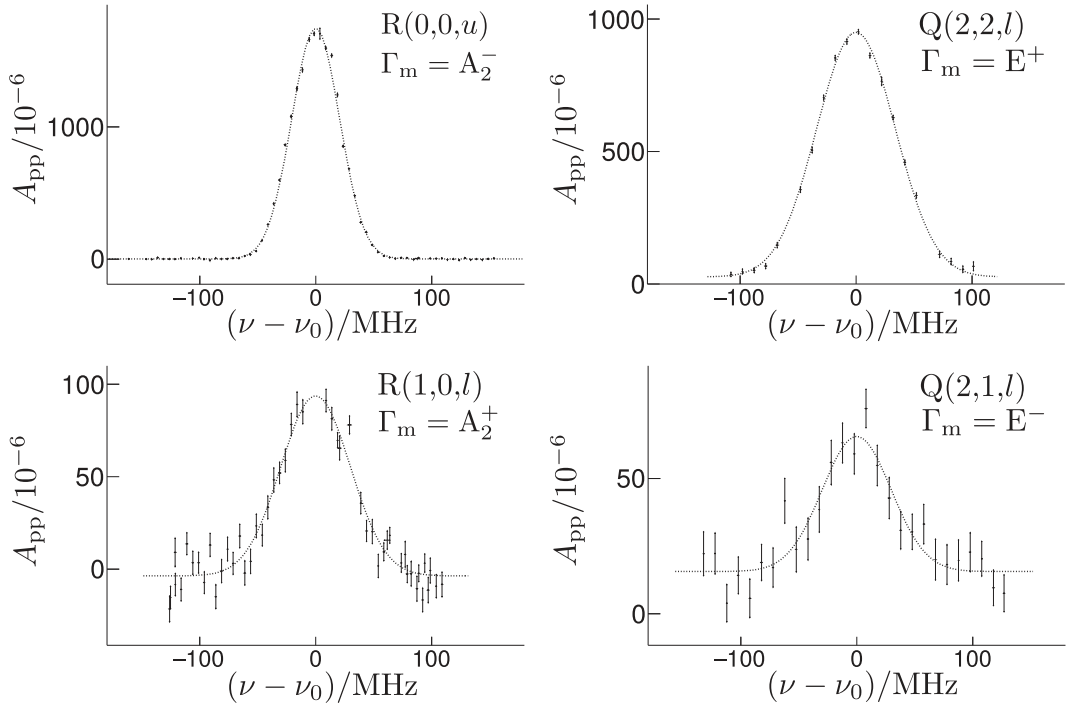

Figure 16. *Left top/bottom*: Measured transitions of R(0,0,*u*) with $\tilde{\nu}_0 = 3355.00728(2)(hc)\,\mathrm{cm}^{-1}$ and R(1,0,*l*) with $\tilde{\nu}_0 = 3376.26979(6)(hc)\,\mathrm{cm}^{-1}$ used to determine the effective rotational temperature '1*' of 8.6(1) K for the levels with A-symmetry in Figure 17. *Right top/bottom*: Measured transition Q(2,2,*l*) with $\tilde{\nu}_0 = 3336.71584(2)(hc)\,\mathrm{cm}^{-1}$ and Q(2,1,*l*) with $\tilde{\nu}_0 = 3336.55985(17)(hc)\,\mathrm{cm}^{-1}$ used to determine the effective rotational temperature '5*' of 9.6(1) K for the levels with E-symmetry independently. For these measurements, the distance *H* varies between 3 and 4 mm due to laser cavity realignment introducing some additional systematic uncertainty, which is not the case for the measurements in Figure 14.

nozzle for the sample (and seeding) gas and sensitive cavity-ring down detection. The instrumental resolution and frequency accuracy is about 1 MHz or better, while the effective spectroscopic resolution is essentially determined by the Doppler widths arising from the molecular beam setup. The sensitivity in terms of absorbance is determined by the reflectivity of the mirrors in the cavity, which for the present experiments was $R = 0.9985$, translating into an effective absorption path length ($\tau_0 \cdot c$) of 300 m. The cavity ring-down absorption spectroscopy has the advantage of being able to measure absorptions quantitatively as in any direct spectroscopic absorption experiment and therefore relative integrated line intensities can be obtained accurately allowing for the quantitative analysis of relative populations of quantum states in the supersonic jet expansion. The more sensitive detection by action spectroscopy (e.g. using multiphoton ionisation) reported in our previous work [46] introduces an uncertainty arising from possibly different detection sensitivity when different quantum states are detected.

We have used the present experiment to remeasure accurate line frequencies for NH_3 absorption in the ν_1-fundamental around 3355 cm^{-1} providing a substantial improvement over previously accepted results, which differ by 50–200 MHz for some lines [73,74,84–87], but agree with our previous work (with hyperfine resolution) for the R(0,0,*u*) line at 3355.007 cm^{-1} to within 0.1 MHz.

The second result of our work concerns the question of nuclear spin symmetry conservation in the supersonic jet expansion. As for many other molecules studied in the past ([27–39] and further references cited there), we find that our results are consistent with nuclear spin symmetry conservation and inconsistent with substantial nuclear spin symmetry relaxation, when considering highly dilute seeded beams ($\lesssim$ 0.1% NH_3 in Ar) and low effective rotational temperatures around 6.6 K. The room temperature mole fraction 0.5 of the A and E nuclear spin symmetry isomers is essentially retained in the expansion. This result is also in agreement with general theoretical expectation [1,2] and with theoretical calculations of nuclear spin symmetry relaxation in gaseous NH_3 predicting very slow relaxation even at room temperature [40]. Previous results on this question for NH_3 have been diverging, some being consistent with nuclear spin symmetry conservation [42,43,45,46], while one result showed substantial nuclear spin symmetry relaxation [44]. This latter phenomenon was observed at relatively high mole fractions of NH_3 in Argon (with $x_{NH_3} \approx 5\%$). Similar to findings of H_2O [36,37], this

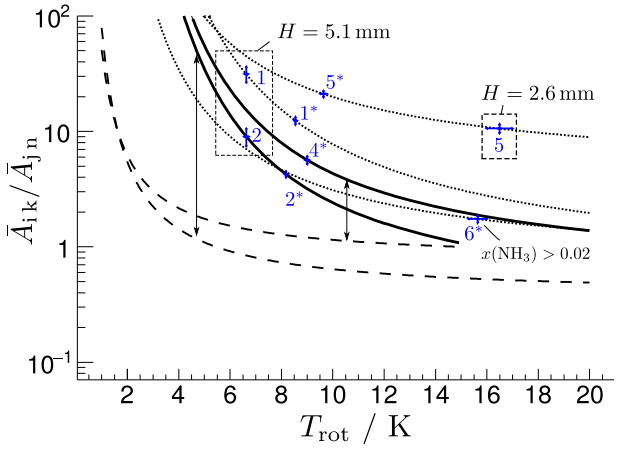

Figure 17. Measured integrated line intensity ratio $\bar{A}_{ik}/\bar{A}_{jn}$ compared to the calculated ratio from Equation (20), assuming nuclear spin symmetry relaxation using Equation (10) and conservation Equation (11) with 1: R(0,0,*u*)/R(1,0,*l*), 2: R(1,1,*l*)/ R(1,0,*l*), 4: Q(1,1,*u*)/P(1,0,*l*), 5: Q(2,2,*l*)/Q(2,1,*l*), 6: R(2,2,*l*)/R(2,1,*l*). The calculated lines give the temperature dependence for each intensity ratio. Ratios of line intensities for the same nuclear spin symmetry (1, 5, and 6) are independent of the relaxation model (shown by dotted lines). Ratios of line intensities for different nuclear spin symmetry (2 and 4) depend on the relaxation model shown as solid lines for nuclear spin symmetry conservation and as dashed lines for complete nuclear spin symmetry relaxation. Ratio 6 possesses a high mole fraction of about 0.02 and Ratio 5 with $H =$ 2.6(2) mm a small distance to the slit nozzle causing a higher rotational temperature for both. For the ratios marked with * the distance *H* varies between 3 and 4 mm.

might be due to the formation and redissociation of clusters $(NH_3)_n$ in the experiments of [44]. In such clusters, nuclear spin symmetry change of the monomers can arise by two mechanisms (i) de facto nuclear spin symmetry violation by proton exchange, (ii) de lege nuclear spin symmetry violation from the couplings of nuclear spin functions with the internal motions in the $(NH_3)_n$ clusters, which lead to complex level structures and much higher densities of internal states than in the monomer. These effects are essentially excluded in our experiments, when carried out with low seeding ratios.

One might consider to reproduce the results of [44] by measurements with large mole fractions of NH_3 in Ar, in order to define the nature of cluster formation under these conditions and the possible resulting nuclear spin symmetry relaxation. However, as pointed out for the case of H_2O in Ref. [37], the nature of the clusters formed, their size and their kinetics, not only depends on the mole fraction used but also on details of the experimental setup, the nozzle used, etc. Thus it would be quite difficult to try to reproduce the results of [44] without the relevant information and thus prospects for unambiguous results did not seem good. Thus we did not pursue this further. In any case, our results for low mole fractions x_{NH_3} clearly show nuclear spin symmetry conservation.

Our conclusion on nuclear spin symmetry conservation under these conditions might appear to depend on the assumption of a thermal rotational level distribution leading to an effective low rotational 'temperature' from measuring only very few levels. Indeed, sometimes non-thermal populations have been claimed (and also sometimes found) for more highly excited rotational and vibrational levels in supersonic jet expansions of polyatomic molecules. However, for our experiments this possibility leads to no substantial uncertainty, because we know that the measured A and E levels contain almost all of the total population. Therefore, the A to E ratios obtained at low temperature are not affected by possibly non-thermal populations in higher levels, as they are too low to result in measurable line intensities in our experiment.

Our results also show no restrictions to relaxation between different parities of rotational levels in NH_3 in agreement with general theoretical considerations [1,2] and with collision experiments of NH_3 with Ar [88] and theory for collisions of NH_3 with rare gas atoms [89]. On the other hand, the finding of nuclear spin symmetry conservation is in agreement with the general theory of approximate nuclear spin symmetry conservation in molecular collisions [1,2] and with quantitative calculations on NH_3 [40].

Finally the experimental setup presented here should be useful for future high resolution spectroscopic studies of chiral molecules in supersonic jet expansions. The frequency ranges covered by our laser systems are suitable for molecules for which theoretical calculations and preliminary spectroscopic investigations indicate the possibility of measuring the parity violating energy difference $\Delta_{pv}E$ between the enantiomers by the method of [52] for instance for 1,2-Dithiine $C_4H_4S_2$ [47,90], Trisulfane HSSSH [48,49] and perhaps 1,3-Difluoroallene [51]. While the necessary analysis of rotation-vibration-tunnelling spectra for such molecules is a non-trivial task, the present experimental setup should provide an important step towards such a goal.

Acknowledgments

Our work is supported financially by an ERC Advanced Grant and by an ETH Zurich grant. We also enjoyed discussions with and help and support from Ziqiu Chen, Csaba Fábri, Karen Keppler, Carine Manca Tanner, Roberto Marquardt, Andreas Schneider, Jürgen Stohner, and Daniel Zindel. Special thanks go to Frédéric Merkt for continuous support and to Andres Laso for his important contribution to the construction of the slit nozzle and other aspects of the experimental setup. We dedicate this publication to Richard N. Zare on the occasion of his 80th birthday.

Disclosure statement

No potential conflict of interest was reported by the author(s).

Funding

The initial part of this work was supported by funding from the European Research Council under the European Union's Seventh Frame Work Programme (FP7) 2007-5302013 Grant 20925.

References

[1] M. Quack, Mol. Phys. **34**, 477–504 (1977).
[2] M. Quack, Fundamental Symmetries and Symmetry violations from high Resolution Spectroscopy. in *Handbook of High Resolution Spectroscopy*, edited by M. Quack and F. Merkt (Wiley, Chichester, New York, 2011), Vol. 1, Chap. 18, pp. 659–722.
[3] J. Hacker and M. Quack, editors, *Symmetrie und Asymmetrie in Wissenschaft und Kunst* (Nova Acta Leopoldina, NF, 2016), Vol. 127, No 412, Halle/ Saale Book with contribution from several authors in English and German.
[4] P. Yi, I. Ozier and N.F. Ramsey, J. Chem. Phys. **55**, 5215–5227 (1971).
[5] J. Bordé, C.J. Bordé, C. Salomon, A. Van Lerberghe, M. Ouhayoun and C.D. Cantrell, Phys. Rev. Lett. **45**, 14–17 (1980).
[6] H. Kanamori, Z.T. Dehghani, A. Mizoguchi and Y. Endo, Phys. Rev. Lett. **119**, 173401 (2017).
[7] J.P. Pique, F. Hartmann, R. Bacis, S. Churassy and J.B. Koffend, Phys. Rev. Lett. **52**, 267–270 (1984).
[8] A.D.J. Critchley, A.N. Hughes and I.R. McNab, Phys. Rev. Lett. **86**, 1725–1728 (2001).
[9] A.D.J. Critchley, A.N. Hughes, I.R. McNab and R.E. Moss, Mol. Phys. **101**, 651–661 (2003).
[10] K.F. Bonhoeffer and P. Harteck, Naturwissenschaften **17**, 182 (1929).
[11] K.F. Bonhoeffer and P. Harteck, Z. Phys. Chem. B **4**, 113–141 (1929).
[12] R.F. Curl, J.V.V. Kasper and K.S. Pitzer, J. Chem. Phys. **46**, 3220–3228 (1967).
[13] K.S. Pitzer, Ann. Rev. Phys. Chem. **38**, 1–25 (1987).
[14] P.L. Chapovsky and L.J.F. Hermans, Ann. Rev. Phys. Chem. **50**, 315–345 (1999).
[15] T. Oka, in *Handbook of High-Resolution Spectroscopy*, edited by M. Quack and F. Merkt (John Wiley & Sons, Ltd., Chichester, 2011) Vol. 1, pp. 633–658.
[16] R.L. Redington and D.E. Milligan, J. Chem. Phys. **37**, 2162–2166 (1962).
[17] L. Fredin and B. Nelander, Chem. Phys. **60**, 181–186 (1981).
[18] F.H. Frayer and G.E. Ewing, J. Chem. Phys. **48**, 781–792 (1968).
[19] B. Gauthier-Roy, L. Abouaf-Marguin and P. Boissel, J. Chem. Phys. **98**, 6827–6834 (1993).
[20] P. Boissel, B. Gauthier-Roy and L. Abouaf-Marguin, J. Chem. Phys. **98**, 6835–6842 (1993).
[21] L. Abouaf-Marguin, A.-M. Vasserot, C. Pardanaud and X. Michaut, Chem. Phys. Lett. **447**, 232–235 (2007).
[22] L. Abouaf-Marguin, A.-M. Vasserot, C. Pardanaud, J. Stienlet and X. Michaut, Chem. Phys. Lett. **454**, 61–64 (2008).
[23] C. Pardanaud, A.-M. Vasserot, X. Michaut and L. Abouaf-Marguin, J. Mol. Struct. **873**, 181–190 (2008).
[24] L. Abouaf-Marguin, A.-M. Vasserot and C. Pardanaud, J. Chem. Phys. **130**, 054503 (2009).
[25] L. Abouaf-Marguin, A.-M. Vasserot, C. Pardanaud and X. Michaut, Chem. Phys. Lett. **480**, 82–85 (2009).
[26] Y. Miyamoto, M. Fushitani, D. Ando and T. Momose, J. Chem. Phys. **128**, 114502 (2008).
[27] H.R. Dübal, M. Quack and U. Schmitt, Chimia **38**, 438–439 (1984).
[28] A. Amrein, M. Quack and U. Schmitt, J. Phys. Chem. **92**, 5455–5466 (1988).
[29] M. Snels, V. Horká-Zelenková, H. Hollenstein and M. Quack, *High Resolution FTIR and Diode Laser Spectroscopy of Supersonic Jets*, in Handbook of High-resolution Spectroscopy edited by M. Quack and F. Merkt (Wiley, Chichester, New York, 2011), Vol. 2, Chap. 27, pp. 1021–1067.
[30] M. Hepp, G. Winnewisser and K. Yamada, J. Mol. Spectrosc. **164**, 311–314 (1994).
[31] M. Hippler and M. Quack, J. Chem. Phys. **116**, 6045–6055 (2002).
[32] C. Manca Tanner and M. Quack, Mol. Phys. **110**, 2111–2135 (2012).
[33] H.M. Niederer, S. Albert, S. Bauerecker, V. Boudon, G. Seyfang and M. Quack, Farad. Discuss. Chem. Soc. **150**, 128–130 (2011).
[34] Z. Bjelobrk, C. Manca Tanner and M. Quack, Z. Phys. Chem. **229**, 1575–1607 (2015).
[35] C. Manca Tanner, M. Quack and D. Schmidiger, Faraday. Discuss. **150**, 118–122 (2011).
[36] C. Manca Tanner, M. Quack and D. Schmidiger, J. Phys. Chem. A **117**, 10105–10118 (2013).
[37] C. Manca Tanner, M. Quack and D. Schmidiger, Mol. Phys. **116**, 3718–3730 (2018).
[38] R. Georges, X. Michaut, A. Moudens, M. Goubet, O. Pirali, P. Soulard, P. Asselin, T. Huet, P. Roy, M. Fournier and A. Vigasin, J. Phys. Chem. A **121**, 7455–7468 (2017).
[39] V. Horká-Zelenková, G. Seyfang, P. Dietiker and M. Quack, J. Phys. Chem. A **123**, 6160–6174 (2019).
[40] P. Cacciani, J. Cosléou, M. Khelkhal, M. Tudorie, C. Puzzarini and P. Pracna, Phys. Rev. A **80**, 042507 (2009).
[41] C. Fábri, R. Marquardt, A. Császár and M. Quack, J. Chem. Phys. **150**, 014102–1–22 (2019) (and to be published).
[42] B.D. Kay and A. Grimley, Chem. Phys. Lett. **127**, 303–308 (1986).
[43] N. Dam, C. Liedenbaum, S. Stolte and J. Reuss, Chem. Phys. Lett. **136**, 73–80 (1987).
[44] M. Hepp, G. Winnewisser and K. Yamada, J. Mol. Spectrosc. **153**, 376–384 (1992).
[45] A. Bach, J.M. Hutchison, R.J. Holiday and F.F. Crim, J. Chem. Phys. **116**, 4955–4961 (2002).
[46] P. Dietiker, E. Miloglyadov, M. Quack, A. Schneider and G. Seyfang, J. Chem. Phys. **143**, 244305 (2015).
[47] S. Albert, I. Bolotova, Z. Chen, C. Fábri, L. Horný, M. Quack, G. Seyfang and D. Zindel, Phys. Chem. Chem. Phys. **18**, 21976–21993 (2016).
[48] S. Albert, I. Bolotova, Z. Chen, C. Fábri, M. Quack, G. Seyfang and D. Zindel, Phys. Chem. Chem. Phys. **19**, 11738–11743 (2017).
[49] C. Fábri, L. Horný and M. Quack, Chem. Phys. Chem. **16**, 3584–3589 (2015).

[50] L. Horný and M. Quack, Mol. Phys. **113**, 1768–1779 (2015).
[51] M. Gottselig and M. Quack, J. Chem. Phys. **123**, 84305–1–84305–11 (2005).
[52] M. Quack, Chem. Phys. Lett. **132**, 147–153 (1986).
[53] K. Keppler, G. Wichmann, E. Miloglyadov, G. Seyfang and M. Quack, *Proceedings of the 26th Colloquium on High-Resolution Molecular Spectroscopy*, Contribution N33 (Dijon, 2019). p. 360.
[54] G. Wichmann, E. Miloglyadov, G. Seyfang and M. Quack, Chimia **73**, 631 (2019) Supplementary PC-170.
[55] M. Hippler and M. Quack, Chem. Phys. Lett. **314**, 273–281 (1999).
[56] Y.B. He, M. Hippler and M. Quack, Chem, Phys. Lett. **289**, 527–534 (1998).
[57] A. O'Keefe and D. A. G. Deacon, Rev. Sci. Instr. **59**, 2544–2551 (1988).
[58] P. Zalicki and R. N. Zare, J. Chem. Phys. **102**, 2708–2717 (1995).
[59] B. A. Paldus and R. N. Zare, in Cavity Ring-Down Spectroscopy, an ultrafast measurement technique, ed. K. Busch and M. B. eds., ch. 1, pp. 1–6 and 49–70, ACS Symposium Series 720, 1999.
[60] B. A. Paldus, C. C. Harb, T. G. Spence, R. N. Zare, C. Gmachl, F. Capasso, D. L. Sivco, J. N. Baillargeon, A. L. Hutchinson and A. Y. Cho, Opt. Lett. **25**, 666–668 (2000).
[61] H. A. Rypkema, M. R. Martin and R. N. Zare, Mol. Phys. **102**, 1501–1508 (2004).
[62] A. J. Huneycutt, R. N. Casaes, B. J. McCall, C.-Y. Chung, Y.-P. Lee and R. J. Saykally, Chem Phys Chem. **5**, 321–326 (2004).
[63] M. Hippler, L. Oeltjen and M. Quack, J. Phys. Chem. A. **111**, 12659–12668 (2007).
[64] Z. Gouennoun and J. Maier, Electronic Spectroscopy of Transient Molecules, in Handbook of High-Resolution Spectroscopy, ed. M. Quack and F. Merkt, Vol. 2, pp, 1321–1343, Wiley, Chichester, 2011.
[65] P. Birza, T. Motylewski, D. Khoroshev, A. Chirokolava, H. Linnartz and J. Maier, Chem. Phys. **283**, 119–124 (2002).
[66] S. Willitsch, Experimental Methods in cation Spectroscopy, in Handbook of high-Resolution Spectroscopy, ed. M. Quack and F. Merkt, vol. 3, pp. 1691–1712, Wiley, Chichester 2011.
[67] H.C. Longuet-Higgins, Mol. Phys. **6**, 445–460 (1963).
[68] M. Schnell, *Group Theory for High-Resolution Spectroscopy of Nonrigid Molecules*, in Handbook of High-resolution Spectroscopy edited by M. Quack and F. Merkt (John Wiley & Sons, Ltd., Chichester, 2011), Vol. 1, pp. 607–632.
[69] M. Snels, L. Fusina, H. Hollenstein and M. Quack, Mol. Phys. **98**, 837–854 (2000).
[70] J.E. Bright Wilson, J. Decius and P.C. Cross, *Molecular Vibrations: The Theory of Infrared and Raman Vibrational Spectra* (Serie Dover Books, New York NY, 1980).
[71] G. Herzberg, *Molecular Spectra and Molecular Structure; II. Infrared and Raman Spectra of Polyatomic Molecules* (D. van Nostrand Company, Inc., Princeton, New Jersey, New York, 1945).
[72] R. Marquardt, K. Sagui, J. Zheng, W. Thiel, D. Luckhaus, S. Yurchenko, F. Mariotti and M. Quack, J. Phys. Chem. A **117**, 7502–7522 (2013).
[73] M.J. Down, C. Hill, S.N. Yurchenko, J. Tennyson, L.R. Brown and I. Kleiner, J. Quant. Spectrosc. Radiat. Transfer **130**, 260–272 (2013).
[74] A.R. Al Derzi, T. Furtenbacher, J. Tennyson, S.N. Yurchenko and A.G. Császár, J. Quant. Spectrosc. Radiat. Transfer **161**, 117–130 (2015).
[75] S. Urban, J. Quant. Spectrosc. Radiat. Transfer **48**, 675–684 (1992).
[76] V. Špirko and W. Kraemer, J. Mol. Spectrosc. **133**, 331–344 (1989).
[77] M. Beyer, N. Hölsch, J. Hussels, C.-F. Cheng, E.J. Salumbides, K.S.E. Eikema, W. Ubachs, C. Jungen and F. Merkt, Phys. Rev. Lett. **123**, 163002 (2019).
[78] M. Quack, J. Chem. Phys. **82**, 3277–3283 (1985).
[79] J. Fischer, R. Gamache, A. Goldman, L. Rothman and A. Perrin, J. Quant. Spectrosc. Radiat. Transfer **82**, 401–412 (2003).
[80] S. Urban, D. Papousek, V. M. Devi, B. Fridovitch, R. D'Cunha, and K. N. Rao, J. Mol. Spectrosc. **106**, 38–55 (1984).
[81] C. Sousa-Silva, N. Hesketh, S.N. Yurchenko, C. Hill and J. Tennyson, J. Quant. Spectrosc. Radiat. Transfer **142**, 66–74 (2014).
[82] F. Merkt and M. Quack, *Handbook of High-Resolution Spectroscopy; Molecular Quantum Mechanics and Molecular Spectra, Molecular Symmetry, and Interaction of Matter with Radiation* (Wiley, Chichester, New York, 2011), vol. 1, ch. 1, pp. 1–55.
[83] E.R. Cohen, T. Cvitas, J.G. Frey, B. Holmström, K. Kuchitsu, R. Marquardt, I. Mills, F. Pavese, M. Quack, J. Stohner, H.L. Strauss, M. Takami and A.J. Thor, *Quantities, Units and Symbols in Physical Chemistry*, 3rd ed. (IUPAC and Royal Society of Chemistry, RSC Publishing, Cambridge, 2007).
[84] G. Guelachvili, A. Abdullah, N. Tu, K.N. Rao, Š. Urban and D. Papoušek, J. Mol. Spectrosc. **133**, 345–364 (1989).
[85] R. Angstl, H. Finsterhoelzl, H. Frunder, D. Illig, D. Papoušek, P. Pracna, K.N. Rao, H. Schroetter and Š. Urban, J. Mol. Spectrosc. **114**, 454–472 (1985).
[86] A. Pine and M. Dang-Nhu, J. Quant. Spectrosc. Radiat. Transfer **50**, 565–570 (1993).
[87] I. Kleiner, L. Brown, G. Tarrago, Q.-L. Kou, N. Picqué, G. Guelachvili, V. Dana and J.-Y. Mandin, J. Mol. Spectrosc. **193**, 46–71 (1999).
[88] J. Schleipen, J. ter Meulen, G. van der Sanden, P. Wormer and A. van der Avoird, Chem. Phys. **163**, 161–172 (1992).
[89] J. Loreau and A. van der Avoird, J. Chem. Phys. **143**, 184303 (2015).
[90] S. Albert, F. Arn, I. Bolotova, Z. Chen, C. Fábri, G. Grassi, P. Lerch, M. Quack, G. Seyfang, A. Wokaun and D. Zindel, J. Phys. Chem. Lett. **7**, 3847–3853 (2016).
[91] L.H. Coudert and E. Roueff, Astron. Astrophys. **449**, 855–859 (2006).
[92] A. Yachmenev and J. Küpper, J. Chem. Phys. **147**, 141101 (2017).
[93] P.A. Coles, A. Owens, J. Küpper and A. Yachmenev, Astrophys J. **870**, 24 (2018).

Appendices

Appendix 1. List of measured lines

One can interpret also the Doppler width as an effective translational temperature along the laser cavity mode, which is mainly perpendicular to the gas expansion and along the slit nozzle exit, with

$$\Delta\nu_{\mathrm{FWHM}} = \sqrt{\frac{8\,k\,T_{\mathrm{trans}}\,\ln 2}{mc^2}}\nu_0 = 1.73\cdot 10^{-7}\cdot\sqrt{T_{\mathrm{trans}}/K}\cdot\nu_0 \tag{A1}$$

$\Delta\nu_{\mathrm{FWHM}}$ is the Doppler width and ν_0 is the transition frequency from Equation (21), k is the Boltzmann constant, m is the mass of NH_3, c is the speed of light, and T_{trans} is the apparent translational temperature. With this a Doppler width of about 50 MHz corresponds to a translational temperature of 8.3 K in qualitative agreement with the carefully obtained effective rotational temperatures in Section 4.3. However, the 'translational temperatures' are strongly affected by the geometry of the expansion and are not to be interpreted as a translational Boltzmann equilibrium, very different from the situation for the rotational temperature.

Table A1. Complete fit result of all measured transitions to the Gauss function from Equation (21).

	Γ_m	mixID	$\tilde{\nu}_0/\mathrm{cm}^{-1}$	$\bar{A}$	$\Delta\nu_{\mathrm{FWHM}}$/MHz	$A_{\max}/10^{-6}$	$A_{\mathrm{BG}}/10^{-6}$	T_{trans}/K	$\bar{\chi}^2$	d.o.f
R(1,0,l)	A_2^+	1	3376.26979(6)	0.070(5)	70.7(28)	97.3(30)	−3.6(14)	16.2(13)	2.2	46
R(0,0,u)	A_2^-	1	3355.00728(2)	0.863(8)	48.8(2)	1744.2(86)	0.8(7)	7.8(1)	2.8	57
Q(2,1,l)	E^-	2	3336.55985(17)	0.035(2)	70.0(98)	49.9(43)	15.6(23)	16.2(45)	1.1	23
Q(2,2,l)	E^+	2	3336.71584(2)	0.747(14)	79.9(9)	923.6(69)	26.6(53)	21.1(5)	2.0	16
Q(1,1,l)	E^-	3	3336.95157(2)	0.377(0)	51.3(7)	725.8(95)	4.2(24)	8.7(2)	2.1	16
R(1,1,l)	E^-	3	3376.32580(2)	0.630(13)	61.7(7)	1008.0(88)	2.3(52)	12.3(3)	4.9	16
R(1,0,l)	A_2^+	3	3376.26964(3)	0.148(7)	64.2(17)	227.8(44)	4.2(27)	13.3(7)	1.2	19
Q(1,1,u)	E^+	4	3335.17135(1)	0.231(0)	51.2(5)	445.1(36)	1.8(11)	8.7(2)	1.6	58
P(1,0,l)	A_2^+	4	3317.20725(7)	0.041(3)	72.8(33)	55.5(20)	0.5(10)	17.7(16)	1.6	49
R(0,0,u)	A_2^-	5	3355.00723(2)	0.473(2)	54.0(6)	864.5(69)	3.5(21)	9.5(2)	2.5	34
P(1,0,l)	A_2^+	6	3317.20722(2)	0.342(5)	67.7(5)	499.0(29)	29.1(14)	15.3(2)	4.8	48
P(1,0,l)	A_2^+	7	3317.20730(2)	0.139(3)	61.0(8)	225.4(24)	12.0(9)	12.5(3)	2.5	51
Q(2,1,l)	E^-	8	3336.56022(7)	0.092(8)	83.8(46)	108.3(41)	20.1(34)	23.2(25)	1.0	16
R(2,2,l)	E^+	9	3395.76457(3)	0.262(7)	79.2(11)	327.3(39)	55.8(20)	20.0(6)	3.8	45
R(2,1,l)	E^-	9	3395.59851(7)	0.151(8)	92.3(27)	161.1(34)	60.3(23)	27.2(16)	6.6	29
Q(3,3,l)	A_2^-	10	3336.39017(4)	0.368(9)	98.2(14)	370.4(34)	78.9(29)	31.9(9)	7.2	24
Q(2,2,l)	E^+	11	3336.71596(2)	0.780(10)	68.4(4)	1125.5(79)	44.0(14)	15.5(2)	7.7	50
Q(2,1,l)	E^-	11	3336.56019(9)	0.074(6)	68.2(31)	106.7(38)	29.2(16)	15.4(14)	5.1	34
R(1,0,l)	A_2^+	12	3376.26957(10)	0.032(5)	61.1(49)	51.5(35)	1.1(19)	12.1(19)	0.9	42
R(1,1,l)	E^-	12	3376.32582(2)	0.287(8)	52.2(8)	543.3(73)	1.8(25)	8.8(3)	2.8	22
R(0,0,u)	A_2^-	12	3355.00725(1)	1.000(12)	51.5(3)	1916.8(105)	7.9(19)	8.7(1)	2.2	23

Notes: The integrated line strength $\bar{A}$ is normalised to the strongest line at the bottom. The stated uncertainty of $\tilde{\nu}_0$, given in parentheses in terms of the last digits given, is defined in Equation (22). All other stated uncertainties in parentheses are the standard uncertainty from the fit. For some measured lines, the reduced χ^2 deviates strongly from 1, but the description from Equation (21) is still sufficient for the conclusions considered in this work.

Note added in proof: After the present publication was in press, a revision of the MARVEL analysis appeared, which reduces some of the discrepancies, but some discrepancies still remain large (T. Furtenbacher, P.A. Coles, J. Tennyson, S.N. Yurchenko, S. Yu, B. Druin, R. Tobias, A. Csaszar, J. Quant. Spectrosc. Radiat. Transfer 251, 107027(2020)).

Appendix 2. Hyperfine transitions

Table A2. Because the table VIII in Ref. [46] was misprinted by exchange of some lines we provide here the complete corrected table.

Vib. lev.	$J'_{K'} \leftarrow J''_{K''}$	Hyperfine transition	$\tilde{\nu}$/cm^{-1}	ν/THz	$\Delta\nu_{HFS}$/MHz[g]
ν_1	1_0,s $\leftarrow$ 0_0,a	$F' = 1 \leftarrow F'' = 1$	3355.007220	100.58058612	−1.006
ν_1	1_0,s $\leftarrow$ 0_0,a	$F' = 2 \leftarrow F'' = 1$	3355.007261	100.58058733	0.201
ν_1	1_0,s $\leftarrow$ 0_0,a	$F' = 0 \leftarrow F'' = 1$	3355.007321	100.58058914	2.012
ν_1	1_0,s $\leftarrow$ 0_0,a	Line pos.[a),b)]	3355.007254	100.58058713	
ν_1	2_1,s $\leftarrow$ 1_1,a	$F' = 2 \leftarrow F'' = 1$	3374.551263	101.16650263	−1.016
ν_1	2_1,s $\leftarrow$ 1_1,a	$F' = 2 \leftarrow F'' = 2$	3374.551312	101.16650324	−0.402
ν_1	2_1,s $\leftarrow$ 1_1,a	$F' = 1 \leftarrow F'' = 1$	3374.551325	101.16650364	−0.007
ν_1	2_1,s $\leftarrow$ 1_1,a	$F' = 3 \leftarrow F'' = 2$	3374.551334	101.16650389	0.246
ν_1	2_1,s $\leftarrow$ 1_1,a	$F' = 1 \leftarrow F'' = 0$	3374.551376	101.16650517	1.527
ν_1	2_1,s $\leftarrow$ 1_1,a	Line pos.[a),c)]	3374.551325	101.16650365	
$\nu_3^{\pm1}$	1_1,a $\leftarrow$ 0_0,a	$F' = 1 \leftarrow F'' = 1$	3458.614363	103.6865011	0.515
$\nu_3^{\pm1}$	1_1,a $\leftarrow$ 0_0,a	$F' = 2 \leftarrow F'' = 1$	3458.614342	103.6866494	−0.103
$\nu_3^{\pm1}$	1_1,a $\leftarrow$ 0_0,a	$F' = 0 \leftarrow F'' = 1$	3458.614311	103.68664856	−1.031
$\nu_3^{\pm1}$	1_1,a $\leftarrow$ 0_0,a	Line pos.[a),d)]	3458.614438	103.6866524	
$2\nu_4^0$	1_0,s $\leftarrow$ 0_0,a	$F' = 1 \leftarrow F'' = 1$	3235.914445	97.0102754	−1.022
$2\nu_4^0$	1_0,s $\leftarrow$ 0_0,a	$F' = 2 \leftarrow F'' = 1$	3235.914486	97.01027576	0.204
$2\nu_4^0$	1_0,s $\leftarrow$ 0_0,a	$F' = 0 \leftarrow F'' = 1$	3235.914547	97.01027760	2.043
$2\nu_4^0$	1_0,s $\leftarrow$ 0_0,a	Line pos.[a),e)]	3235.914479	97.0102756	
$2\nu_4^{\pm2}$	1_1,a $\leftarrow$ 0_0,a	$F' = 1 \leftarrow F'' = 1$	3251.779682	97.48590239	0.517
$2\nu_4^{\pm2}$	1_1,a $\leftarrow$ 0_0,a	$F' = 2 \leftarrow F'' = 1$	3251.779662	97.48590177	−0.103
$2\nu_4^{\pm2}$	1_1,a $\leftarrow$ 0_0,a	$F' = 0 \leftarrow F'' = 1$	3251.779631	97.48590084	−1.034
$2\nu_4^{\pm2}$	1_1,a $\leftarrow$ 0_0,a	Line pos.[a),f)]	3251.779665	97.4859019	

Notes: For details of the hyperfine structure measurements in ν_1 and other levels, we refer to [46]. Further recent discussions of hyperfine structure of NH_3 lines can be found in [91–93].

(a) Doppler broadened superposition, we also give parameters for each group of lines.

(b) eQq(ν_i)/MHz = −4.0246(26)

(c) eQq(ν_i)/MHz = −4.037(55)

(d) eQq(ν_i)/MHz = −4.123(29)

(e) eQq(ν_i)/MHz = −4.0866(35)

(f) eQq(ν_i)/MHz = −4.134(22)

(g) shift with respect to line position as stated.

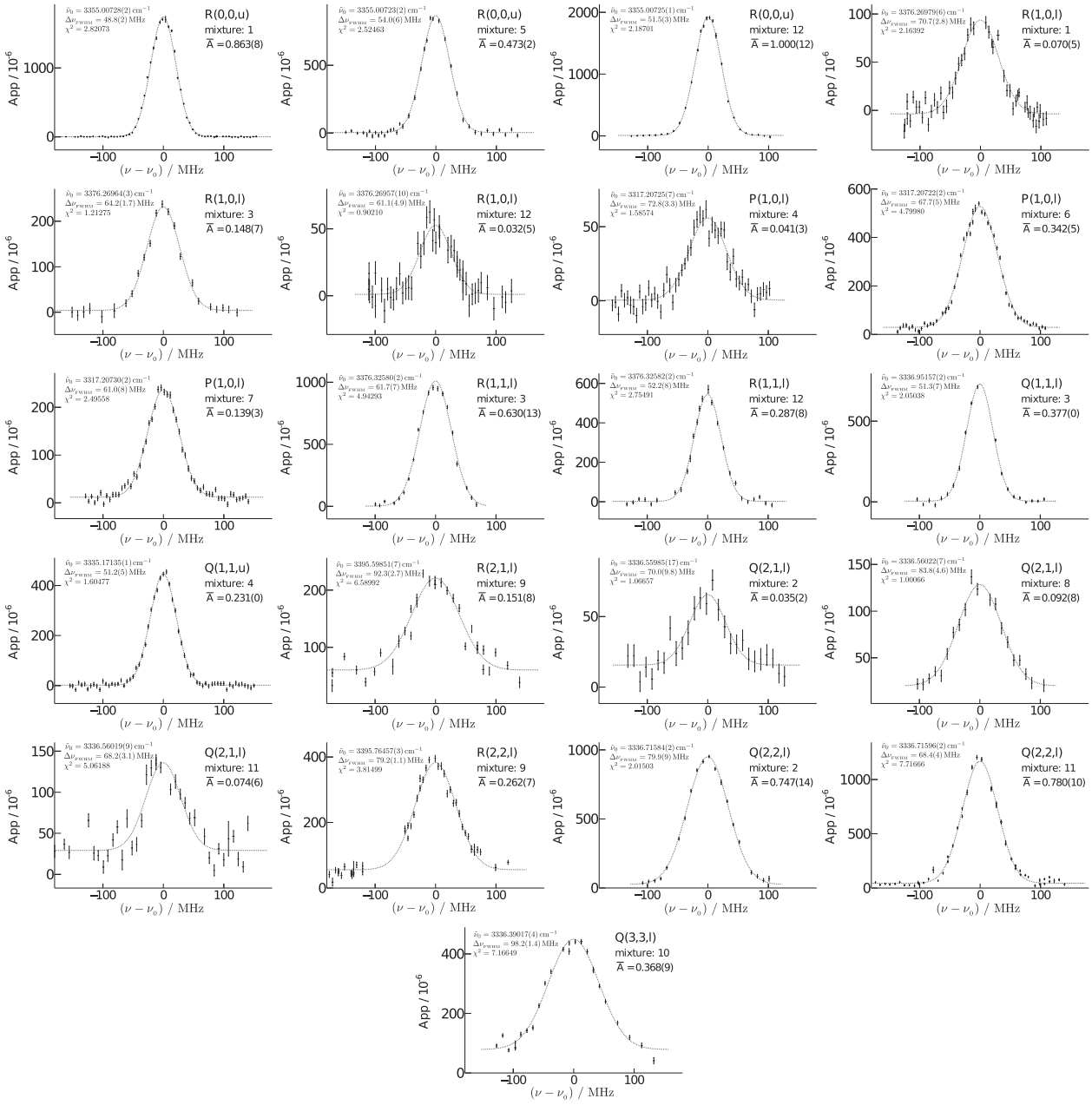

Figure A1. Measured spectral lines with the Gaussian fit from Equation (21). See also Tables 6 and A1 for a list of all measured frequencies and the relevant fit parameters.

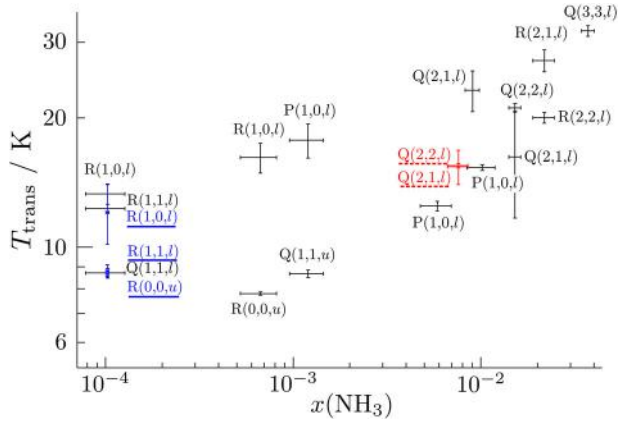

Figure A2. Apparent 'translational temperatures' of the measured spectral lines. The underlined points in blue show the lines with $H = 5.1$ mm and the dashed underlined points in red show the lines with $H = 2.6$ mm. A trend for increased translational temperatures is visible for higher NH_3 concentrations, but also large systematic effects presumably by an uncontrolled variation of H can be seen by two trend lines.